공학박사 학위논문

Synthesis and Characterization of Highly Durable Nanocatalysts by Protecting Active Sites

활성 부위 보호를 통한

내구성이 뛰어난

나노 촉매의 합성과 분석

2016년 8월

서울대학교 대학원

화학생물공학부

Samuel Woojoo Jun

Abstract

Synthesis and Characterization of Highly Durable Nanocatalysts by Protecting Active Sites

Samuel Woojoo Jun

School of Chemical and Biological Engineering

The Graduate School

Seoul National University

At present, the practical application of nanocatalysts is hindered by their low durability. To overcome this limitation, in this thesis, I synthesized highly durable nanocatalysts by protecting the catalyst active sites and then characterized the products. By immobilizing the acid and base catalysts on the nanomaterial surface, I secured the activity

of each acid or base catalyst. In the case of the oxygen reduction reaction (ORR) catalyst, the nanoparticles (NPs) are protected from dissolution and agglomeration under the harsh fuel cell operating conditions by coating the nanocatalyst surface with a thin N-doped carbon shell.

Following the introduction chapter, Chapter 2 describes the successful synthesis of a magnetically separable mesoporous site-isolated acid-base catalyst using a one-pot reaction. The catalyst showed excellent performance with very high yield and selectivity for the conversion of benzaldehyde dimethyl acetal to 1-nitro-2-phenylethylene via benzaldehyde using tandem acid-catalyzed deacetalization and base-catalyzed Henry reaction. The catalyst could be easily recovered using a magnet and dispersed in subsequent reaction mixtures, enabling recycling of the catalyst for up to five uses without loss of catalytic activity. Furthermore, comparative studies reveal that the larger-pore materials exhibited higher catalytic activity than the smaller-pore materials.

In Chapter 3, I present the synthesis of highly durable and active intermetallic ordered face-centered tetragonal (fct)-PtFe NPs coated with a “dual-purpose” N-doped carbon shell. Ordered fct-PtFe NPs with a size

of only a few nanometers were obtained by the thermal annealing of polydopamine-coated PtFe NPs, and the N-doped carbon shell formed *in situ* from the dopamine coating could effectively prevent the coalescence of NPs. This carbon shell also protects the NPs from detachment and agglomeration as well as dissolution under the harsh fuel cell operating conditions. By controlling the thickness of the shell below 1 nm, I achieved excellent protection of the NPs as well as high catalytic activity, as the thin carbon shell is highly permeable for the reactant molecules. The mass activity and specific activity of the ordered fct-PtFe/C nanocatalyst coated with an N-doped carbon shell are 11.4 and 10.5 times higher, respectively, than those of a commercial Pt/C catalyst. Moreover, a membrane electrode assembly (MEA) fabricated using this catalyst exhibited long-term stability for 100 h without significant activity loss. *In situ* X-ray absorption near edge structure (XANES) and energy-dispersive X-ray spectroscopy (EDS) studies confirmed that the ordered fct-PtFe structure is critical for the long-term stability of this nanocatalyst. The strategy developed herein, namely, utilizing an N-doped carbon shell to obtain small ordered-fct PtFe nanocatalysts and

protect the catalyst during fuel cell cycling, is expected to provide a simple and effective route for the commercialization of fuel cells.

Keywords: Nanocatalyst, Synthesis, Magnetic mesoporous, Acid-base catalyst, Cooperative catalyst, Tandem reaction, Carbon coating, Electrocatalyst, Ordered intermetallic, Oxygen reduction reaction.

Student Number: 2009-23956

Contents

List of Tables

List of Schemes

List of Figures

Chapter 1. Introduction:

Strategies for Increasing Catalyst Durability by the Immobilization and Passivation of Active Sites

1.1 Introduction

Nanoscience has captured the attention of many researchers as a means of developing novel and useful materials, and a tremendous amount of research has been conducted in this field over the last two decades. Since Bawendi and colleagues reported the first colloidal synthesis of quantum dot nanoparticles (NPs),[1] many efforts have been made to apply various kinds of nanomaterials in the energy[2] and biomedical[3] fields. In particular, these innovative particles have demonstrated versatility in the field of heterogeneous catalysis. The greatest advantage of using nanoparticles as catalysts is their extremely

high surface-to-volume ratio.[4] Because catalytic reactions occur on the catalyst surface, mass activity is critical for catalyst efficiency.

Catalyst efficiency is also strongly dependent on the durability and long-term stability of the catalyst, as replacing or regenerating a used catalyst can be costly, time-consuming, or labor-intensive. Especially on an industrial scale, catalyst efficiency is intimately related to cost effectiveness. Although nanocatalysis is a well-established field of research, catalyst inactivation due to damage incurred during reaction remains problematic.[5]

One widely accepted strategy for enhancing catalyst durability is fixing the catalyst on a rigid support. Immobilizing a fragile catalyst on a robust support prevents unnecessary interaction between the catalysts and facilitates separation after the reaction, minimizing catalyst loss. This strategy is critical for achieving good performance using "wolf-and-lamb" type reaction catalysis,[6] which involves two mutually incompatible catalysts (e.g., an acid catalyst and a base catalyst) (**Figure 1.1**). Choosing mesoporous materials or nanomaterials as the catalyst support can allow researchers to take advantage of the benefits associated with their extremely high surface area per mass.[7] If the support material

is magnetically responsive, the separation step becomes much easier, which also decreases the cost of the industrial-scale process.[8]

Another strategy for improving the catalyst durability is coating a protective layer on the catalyst surface. These coatings make the catalyst more resistant to detachment and agglomeration, the major deactivation mechanisms during the catalytic reaction. The key property of the shell is its permeability to the reactant, as a shell that hinders the ability of the reactant to reach the active site of catalyst will decrease the catalyst efficiency. In this regard, carbon materials, whose pores are large enough for the reactants to penetrate, are very promising as protective layers for catalysts.[9]

In the remainder of this chapter, I discuss two methods of enhancing the catalyst durability. In Section 1.2, I summarize the literature on catalyst immobilization on the surface of a nanomaterials. Next, in Section 1.3, I summarize the literature on catalyst passivation via a protective layer. Finally, Section 1.4 provides an overview of the thesis as a whole.

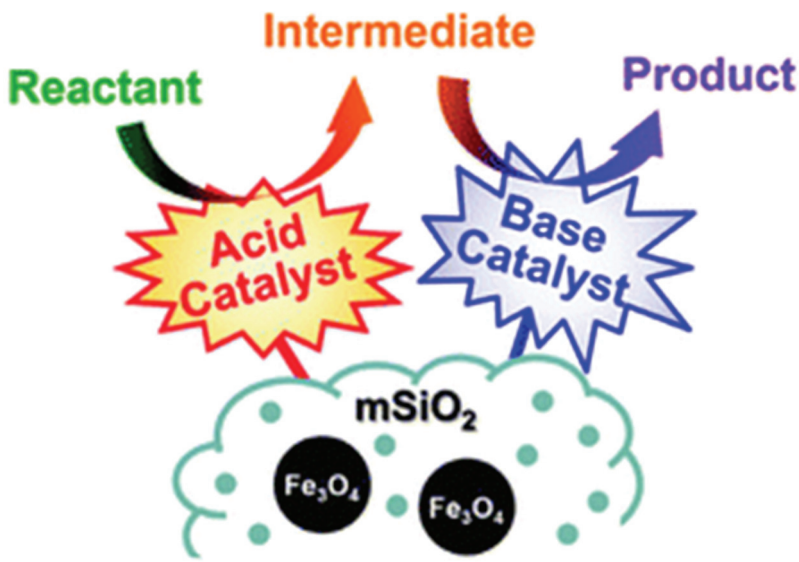

Figure 1.1 Magnetically separable "wolf-and-lamb" type reaction catalyst

1.2 Catalyst Immobilization on the Nanomaterials

Catalysis research can be divided into two fields: homogenous and heterogeneous catalysis. The major difference between these fields is whether the catalyst and reactants react in the same phase or in different phases. Because homogenous catalysts are molecular-scale and easily soluble in media, reactants can conveniently access active sites, leading high catalytic activity. Furthermore, the catalyst structure can be easily modified, providing endless potential for application. However, their difficult separation after use is a major hurdle to their wide applications in industry. One well-accepted strategy for overcoming these disadvantages is immobilization of the homogeneous catalysts on nanomaterials. Among the various catalyst supports, magnetic mesoporous materials are considered one of the best candidates. Examples of these materials are described below.

1.2.1 Magnetically Separable Mesoporous Nanocatalysts

Magnetic mesoporous nanomaterials have attracted attention due to their facile synthesis, easy modification, and interesting properties.[10]

These materials are most notable for their response to magnetic force and their innumerable potential functionalities accessible via surface modification. Relative to the current trend of using filter or membrane separation methods for catalyst separation (**Figure 1.2**),[11] magnetic separation enhances catalyst durability by preventing damage to the catalyst from unnecessary collision with the filter.

In the most common syntheses of this magnetic mesoporous materials, a magnetic core is prepared and then covered with a mesoporous material; alternatively, magnetic particles are embedded on the surface of a mesoporous substrate synthesized by a conventional method (**Figure 1.3**).[12] Lu et al. reported a synthetic method for a magnetically separable palladium-based nanocatalyst, which is a representative synthetic procedure for nanocatalysts loaded on a magnetic mesoporous support.[13] This procedure consists of five steps (**Figure 1.4**). First, a carbon/SBA-15 composite is synthesized and loaded with cobalt nanoparticles. To protect the magnetic-responsive cobalt nanoparticles, the surface is coated with a thin carbon layer, and then the silica scaffold is removed using hydrofluoric acid to create a porous system. Finally, palladium nanoparticles are deposited for the hydrogenation reaction. The catalytic

activity of the as-synthesized catalyst was found to be robust, and the reaction rate remained at its initial value after multiple recycles. More importantly, complete separation of the catalyst was achieved by simply applying the magnet to the reaction vessel. As described above, there is a strong demand for additional research on the synthesis of catalysts immobilized on magnetic support despite the complexity of this process.

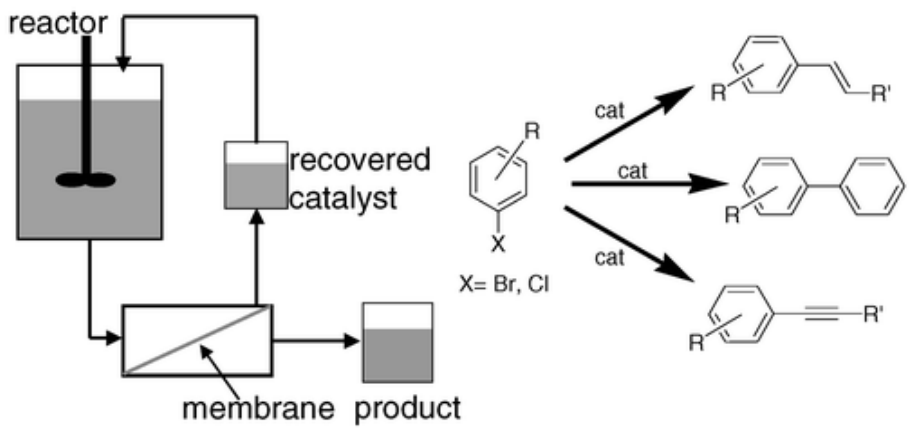

Figure 1.2. Schematic diagram of membrane filtration process. (From Ref. [11], Datta, A.; Ebert, K.; Plenio, H. *Organometallics* **2003**, 22 (23), 4685–4691)

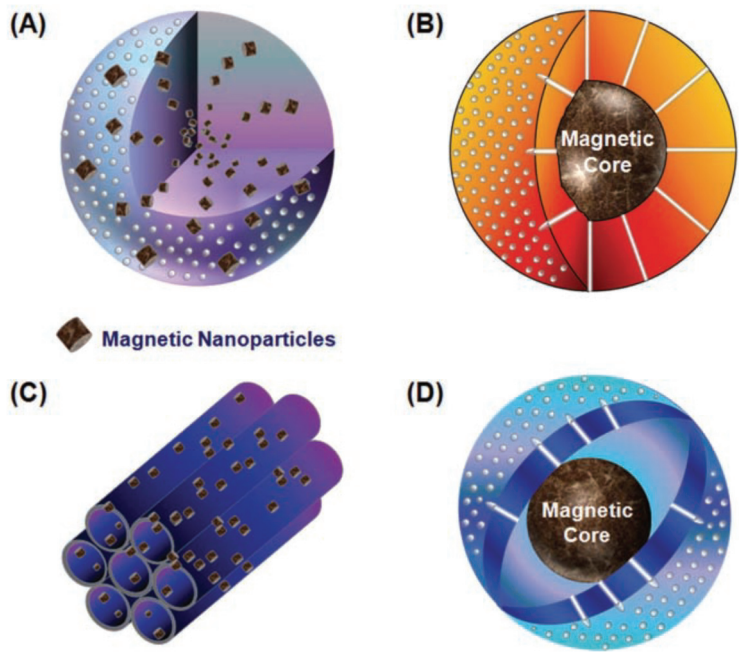

Figure 1.3. Morphologies of magnetic nanoparticle/silica mesoporous material nanocomposites: A) mesoporous silica spheres embedding monodisperese magnetic nanocrystals, B) microspheres encapsulating magnetic cores into perpendicularly aligned mesoporous shells, C) ordered mesoporous materials loaded with magnetic NPs inside the porous channels or cages, and D) rattle-type magnetic nanocomposites. (from Ref. [12], Liu, J.; Qiao, S. Z.; Hu, Q. H.; Lu, G. Q. M. *Small* **2011**, *7* (4), 425–443.)

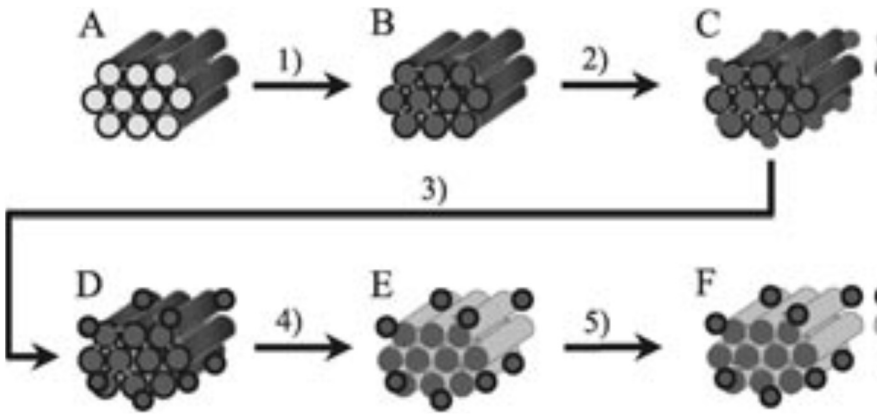

Figure 1.4. Illustration of the synthesis procedure. Materials: A) ordered mesoporous silica SBA-15; B) carbon/SBA-15 composite; C) B with surface-deposited cobalt nanoparticles; D) protected cobalt nanoparticles on C; E) magnetic-ordered mesoporous carbon; F) Pd on E. Procedure: 1) carbonization of the carbon precursor in SBA-15; 2) incorporation of cobalt nanoparticles on B; 3) coating of carbon on cobalt nanoparticles; 4) dissolution of silica to create pore system; 5) loading of Pd in pores to introduce catalytic function. (from Ref [13], Lu, A.; Schmidt, W.; Matoussevitch, N.; Bönnemann, H.; Spliethoff, B.; Tesche, B.; Bill, E.; Kiefer, W.; Schüth, F. Angew. Chemie 2004, 116 (33), 4403–4406.)

1.2.2 Acid-Base Tandem Catalyst

Acid-base site-isolated catalysts, which are inspired by enzymes that effectively perform multistep catalytic reactions through the cooperative interactions of isolated catalytic active sites, have been intensively investigated as single-site heterogeneous catalysts.[14] Several silica nanostructured materials have been employed as heterogeneous supports[15] for the site-isolated immobilization of acidic and basic catalytic species, and many research groups have attempted to improve the catalytic performance by controlling the morphology and structure of the catalysts.[16]

Huang et al. reported the synthesis of an acid-base tandem catalyst by immobilizing the acid and base catalysts on different mesoporous silica nanoparticles to spatially separate these adversarial catalysts (**Figure 1.5**).[17] The immobilization on different supports also allowed the ratio between those catalysts to be easily controlled, facilitating the study of the reaction kinetics. Huang et al. also provided experimental evidence of the importance of catalyst immobilization by showing that the tandem reaction only occurred when both acid and base catalysts were immobilized on the supports.

Yolk-shell type supports are another tool for the spatial separation of acid and base catalysts (**Figure 1.6**).[18] The acid catalysts were immobilized on the outer "shell" surface of the support, whereas the base catalysts were decorated on the inner "yolk" surface. The catalytic activity of this yolk-shell type catalyst was superior to that of a physical mixture of each part. However, spatially separated acid and base catalysts require longer reaction periods than the neighboring-catalyst cases. The above-mentioned catalyst requires over 20 h to achieve complete conversion. Thiel et al. reported the synthesis of an acid-base tandem catalyst by immobilizing acid and base catalysts adjacent to each other (**Figure 1.7**).[19] Their catalyst required only 5 h to achieve complete conversion, and the performance of each catalyst was maintained, without any destruction.

Representative reaction pathways for a cooperative catalyst with two different active sites are shown in **Figure 1.8**.[20] Acid-base tandem catalysts follow sequential activation (**Figure 1.8B**), in which two groups sequentially activate one reagent. As a result, maintaining the gap between the two incompatible catalysts is the key to avoiding catalyst inactivation. Considering the mechanism of this acid-base tandem

reaction (**Figure 1.9**),[21] the product of the acid-catalyzed reaction becomes the starting reagent of the base-catalyzed reaction. Therefore, the overall reaction rate can be increased by shortening the diffusion length of the intermediate, i.e., shortening the distance between the acid and base catalysts. In this regard, the flexibility of the catalyst is also important. Bass et al. suggested that the versatility, and therefore the activity, of the catalyst could be increased by creating various distances between two catalysts (**Figure 1.10**).[22]

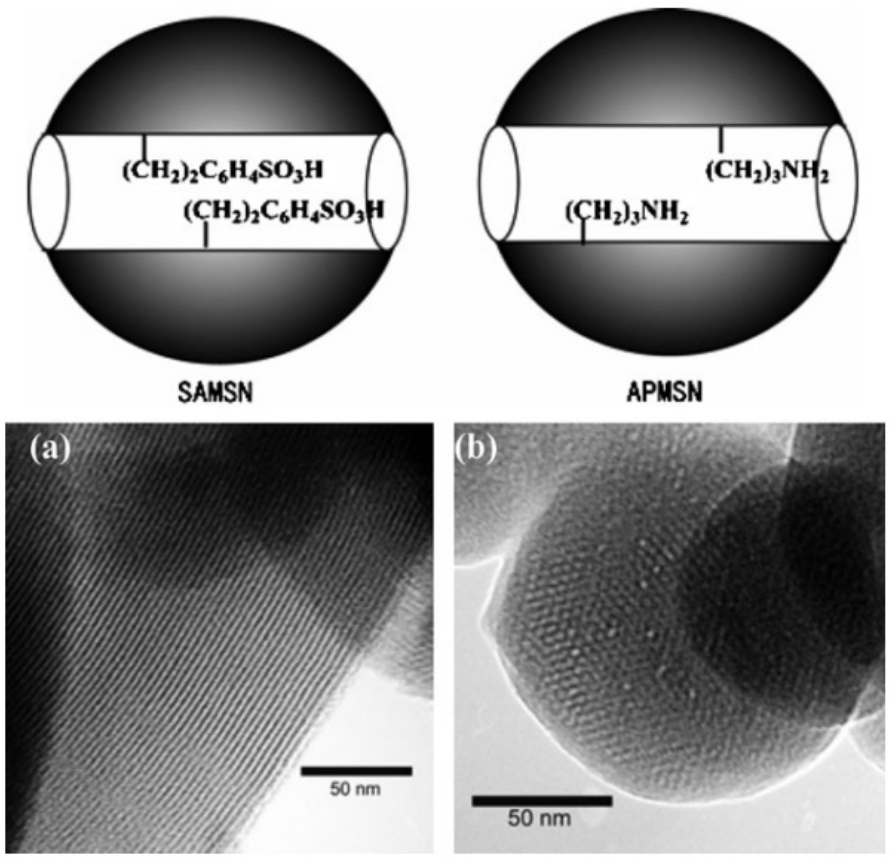

Figure 1.5. Mesoporous silica nanoparticles functionalized with an ethyl-phenylsulfonic acid (SAMSN) or an aminopropyl group (APMSN). Transmission electron microscopy (TEM) images of SAMSN (a) and APMSN (b). Scale bar = 50 nm. (From Ref. [17], Huang, Y.; Trewyn, B. G.; Chen, H.-T.; Lin, V. S.-Y. *New J. Chem.* **2008**, *32* (8), 1311-1313.)

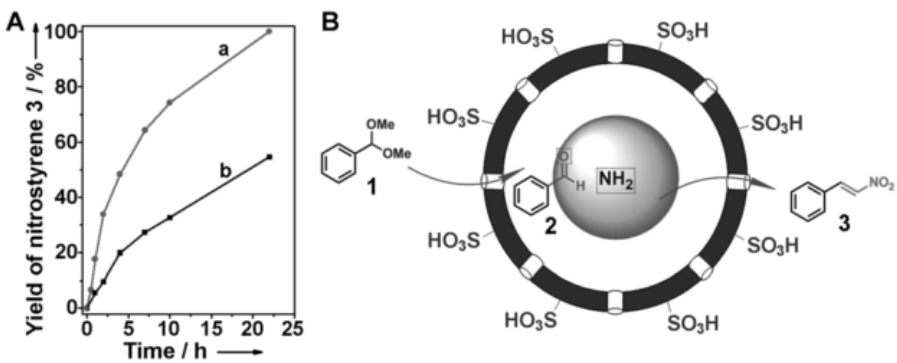

Figure 1.6. Catalytic performance of the YSN nanoreactor. A) The reaction profiles of YS-NH_2@SO_3 H (a), and the mixture (b) of YS-NH_2@ethanesilica and YS-silica@SO_3 H for the deacetalization– Henry cascade reaction. B) Schematic illustration of the cascade reaction in a YS-NH_2 @SO_3 H nanoreactor. (From Ref. [18], Yang, Y.; Liu, X.; Li, X.; Zhao, J.; Bai, S.; Liu, J.; Yang, Q. *Angew. Chem. Int. Ed.*, **2012**, *51* (36), 9164–9168.)

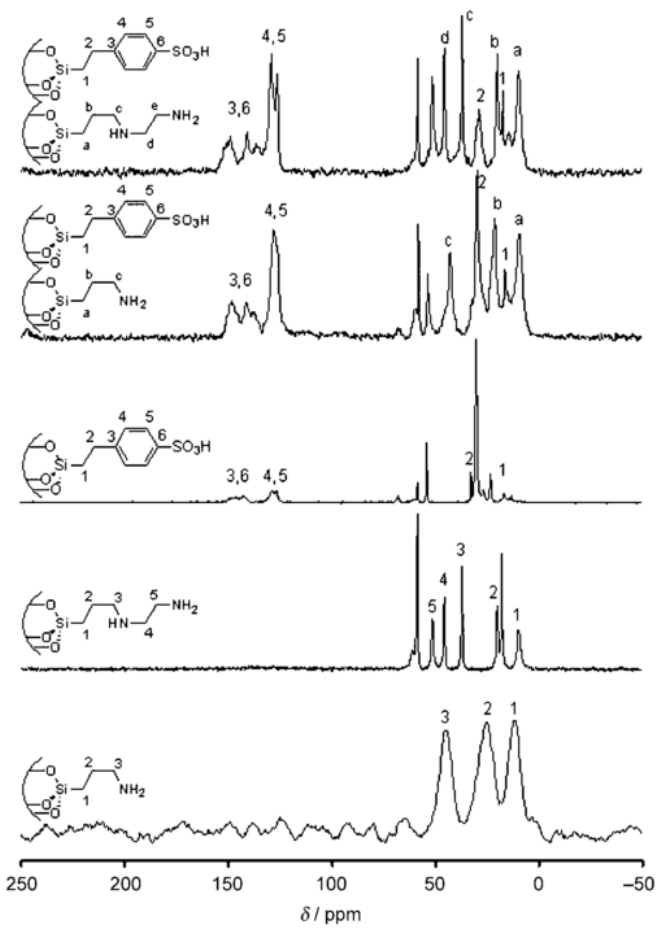

Figure 1.7. ^{13}C CP/MAS NMR spectra of functionalized MSN samples. The unmarked signals denote residual surfactant peaks and ethoxy groups. (From Ref. [19], Shylesh, S.; Wagner, A.; Seifert, A.; Ernst, S.; Thiel, W. R. Chem. Eur. J. 2009, 15 (29), 7052–7062.)

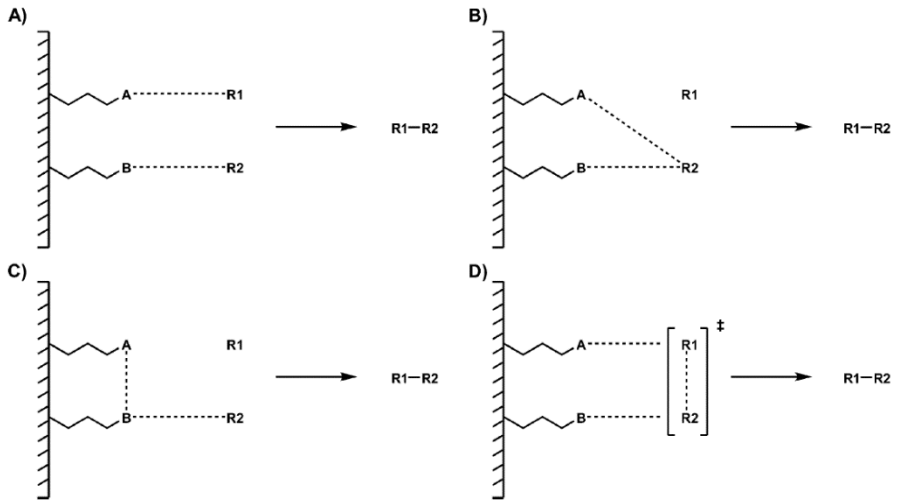

Figure. 1.8. Some possible modes of cooperativity between surface groups A and B in catalyzing the reaction between reactants R1 and R2. (A) Dual activation: A activates R1, and B activates R2. (B) Sequential activation: A activates R2, and B further activates R2. (C) Self-activation: A activates B, and B then activates R2. (D) Multiple-point transition-state stabilization. (From Ref. [20], Margelefsky, E. L.; Zeidan, R. K.; Davis, M. E. *Chem. Soc. Rev.* **2008**, *37* (6), 1118–1126.)

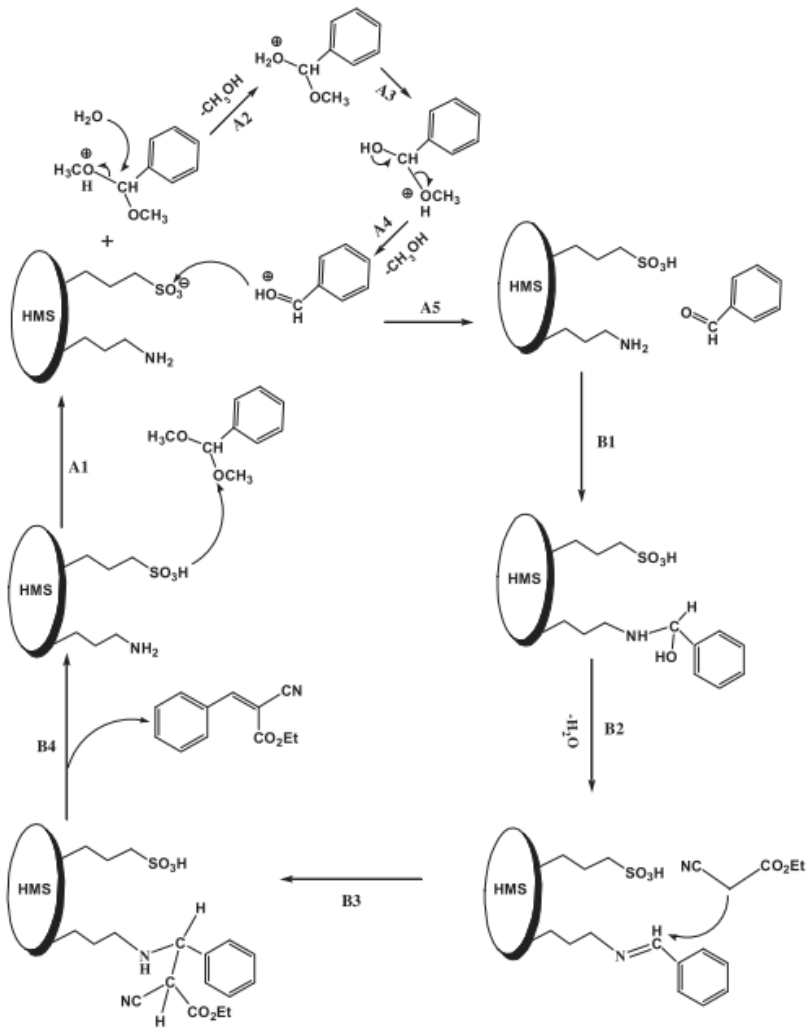

Figure 1.9. Proposed mechanism for the acid-/base-catalyzed one-pot deacetalization–Knoevenagel reaction. (From Ref. [21], Shang, F.; Sun, J.; Wu, S.; Liu, H.; Guan, J.; Kan, Q. *J. Colloid Interface Sci.* **2011**, *355* (1), 190–197.)

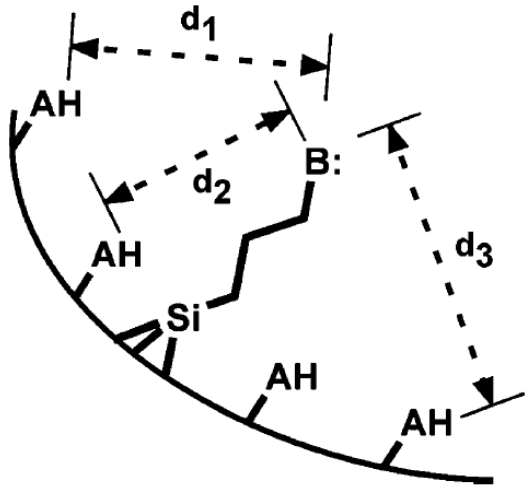

Figure 1.10. Silica surface as a macroscopic ligand providing a range of acid-base distances for bifunctional cooperativity. (From Ref. [22], Bass, J. D.; Solovyov, A.; Pascall, A. J.; Katz, A. *J. Am. Chem. Soc.* **2006**, *128* (11), 3737–3747.)

1.3 Catalyst Passivation by the Carbon Coating

At present, the coating of an electrocatalyst with a carbon material is considered one of the best ways of improving catalyst durability and activity. The natural pores of carbon allow reagents to pass through the shell while still providing physical encapsulation of the core catalyst. In the oxygen reduction reaction (ORR), the major contributors to catalyst damages are the corrosive acidic media and the high positive potential used during operation.[23] Under these conditions, dissolution, detachment, and aggregation of electrocatalyst occur easily. These processes decrease the electrochemically active surface area (ECSA) and therefore the performance (**Figure 1.11**).[24]

Guo et al. reported the synthesis of Pt nanoparticles coated with N-doped porous carbon on carbon nanotubes (**Figure 1.12**), and this structure showed tolerance to harsh conditions, such as accelerated durability testing (ADT) or heat treatment at 900 °C.[25] These researchers attribute the enhanced durability to the electronic interaction between the embedded Pt nanocatalysts and N-doped carbon shell. Pylypenko et al. explained this phenomenon using density functional theory (DFT) simulation and the electron energy loss (EEL) spectra of

an N-implanted high-surface-area carbon support and highly oriented pyrolytic graphite (HOPG) substrate.[26] The use of graphitic N greatly improved the dissolution resistance of Pt and impeded the dissolution of Pt in the case of alloyed substrates (**Figure 1.13**). In the case of pyridinic and pyrrolic N, the improvement of the dissolution resistance worked differently, implying that the synthesis of the N-doped carbon shell must be tailored to the electrocatalyst of interest.

.

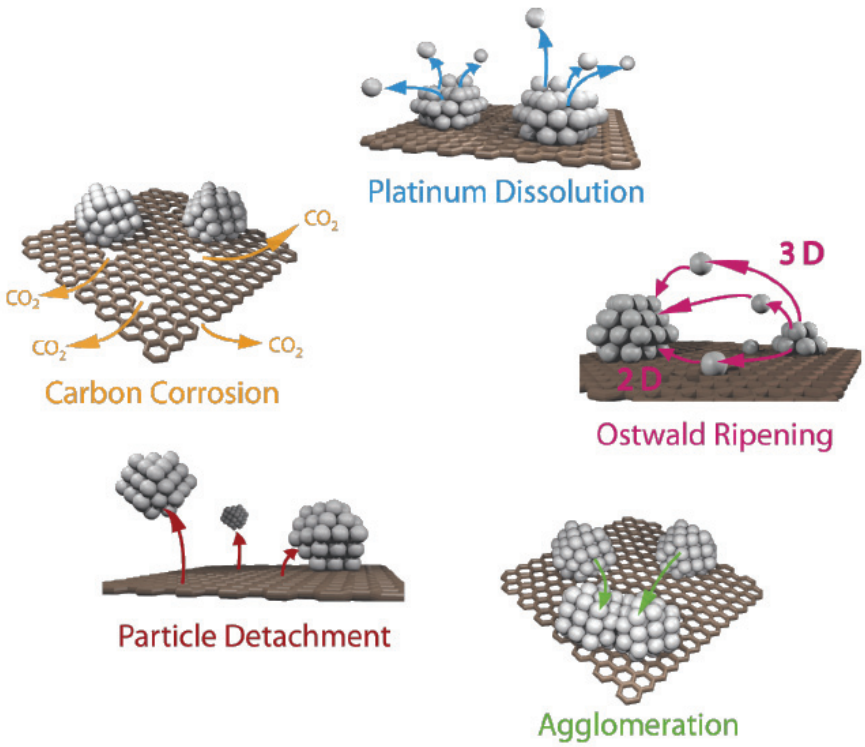

Figure 1.11. Simplified representation of the degradation mechanisms for platinum particles on a carbon support in fuel cells. (From Ref. [24], Meier, J. C.; Galeano, C.; Katsounaros, I.; Witte, J.; Bongard, H. J.; Topalov, A. A.; Baldizzone, C.; Mezzavilla, S.; Schüth, F.; Mayrhofer, K. J. J. Beilstein J. Nanotechnol. 2014, 5 (1), 44–67.)

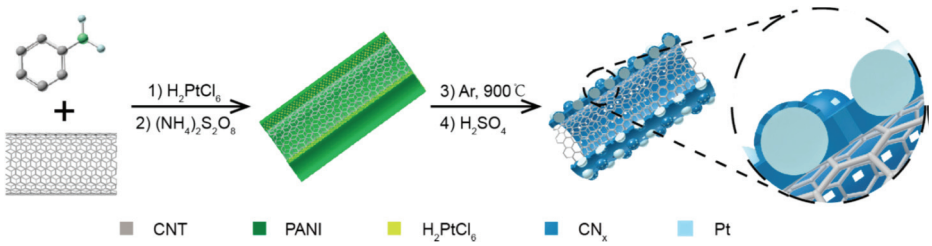

Figure 1.12. Schematic illustration of the preparation of Pt@CNx/CNT catalyst (From Ref. [25], Guo, L.; Jiang, W. J.; Zhang, Y.; Hu, J. S.; Wei, Z. D.; Wan, L. J. ACS Catal. 2015, 5 (5), 2903–2909.)

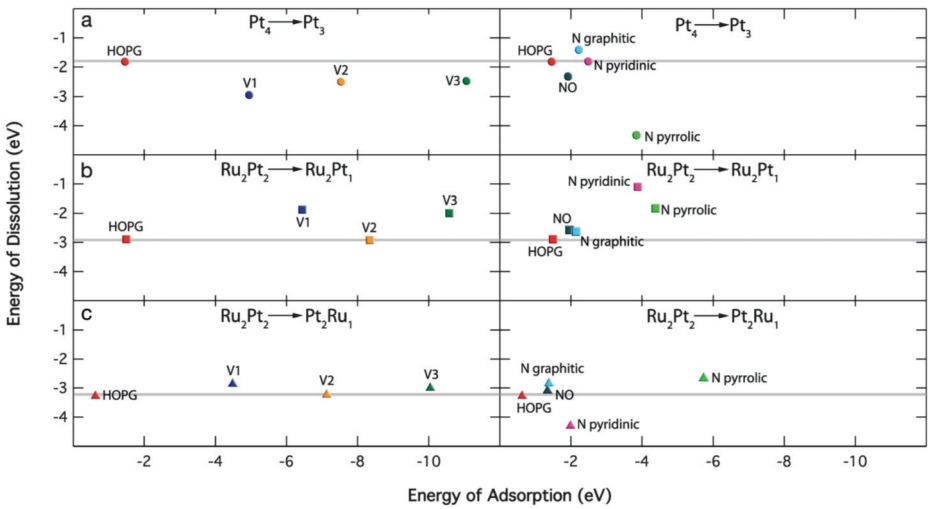

Figure 1.13 Energy of adsorption vs. energy of dissolution for highly oriented pyrolytic graphite (HOPG), vacancies, and N-defects for Pt and PtRu on different HOPG substrates. (a) Pt in Pt; (b) Pt in PtRu; (c) Ru in PtRu. Simulated defects included pyridinic (Npyridinic), pyrrolic (Npyrrolic), graphitic (Ngraphitic), and N–O (NO) nitrogen defects; carbon vacancies (V); and clusters of two (2V) and three (3V) vacancies**.** (From Ref. [26], Pylypenko, S.; Borisevich, A.; More, K. L.; Corpuz, A. R.; Holme, T.; Dameron, A. a.; Olson, T. S.; Dinh, H. N.; Gennett, T.; O'Hayre, R. energy environ. sci 2013, 6 (10), 2957-2964.)

1.4 Dissertation Overview

As described above, the practical application of nanocatalysts requires the development of strategies for increasing their durability. This dissertation focuses on the synthesis and characterization of highly durable nanocatalysts achieved by protecting the active sites of the catalysts. By immobilizing the acid and base catalysts on the nanomaterial surface, I secured the activity of each acid or base catalyst. For the ORR catalyst, the nanoparticles are protected from dissolution and agglomeration under the harsh fuel cell operating conditions by coating a thin N-doped carbon shell on the surface of the nanocatalyst.

In the next part of this thesis, Chapter 2, the successful synthesis of a magnetically separable mesoporous site-isolated acid-base catalyst using a one-pot reaction is described. The catalyst showed excellent performance with very high yield and selectivity for the conversion of benzaldehyde dimethyl acetal to 1-nitro-2-phenylethylene via benzaldehyde using tandem acid-catalyzed deacetalization and base-catalyzed Henry reaction. The catalyst could be easily recovered using a magnet and dispersed in subsequent reaction mixtures, enabling the catalyst to be recycled up to five times without loss of catalytic activity.

Furthermore, comparative studies revealed that the larger-pore materials exhibited higher catalytic activity than the smaller-pore materials.

Later, in Chapter 3, I present the synthesis of highly durable and active intermetallic ordered face-centered tetragonal (fct)-PtFe NPs coated with a "dual-purpose" N-doped carbon shell. Ordered fct-PtFe NPs of only few nanometers in size are obtained by the thermal annealing of polydopamine-coated PtFe NPs, and the N-doped carbon shell formed *in situ* from the dopamine coating could effectively prevent the coalescence of NPs. This carbon shell also protected the NPs from detachment and agglomeration as well as dissolution under the harsh fuel cell operating conditions. By controlling the thickness of the shell below 1 nm, both excellent protection of the NPs as well as high catalytic activity were achieved, as the thin carbon shell was highly permeable for the reactant molecules. The mass activity and specific activity of this ordered fct-PtFe/C nanocatalyst coated with an N-doped carbon shell are 11.4 and 10.5 times higher, respectively, than those of a commercial Pt/C catalyst. Moreover, a membrane electrode assembly (MEA) fabricated using this catalyst demonstrated long-term stability for 100 h without significant activity loss. *In situ* X-ray absorption near edge structure (XANES) and

energy-dispersive X-ray spectroscopy (EDS) studies confirmed that the ordered fct-PtFe structure is critical for the long-term stability of our nanocatalyst. The strategy developed herein, namely, the use of an N-doped carbon shell to obtain a small ordered-fct PtFe nanocatalyst and protect the catalyst during fuel cell cycling, is expected to provide a simple and effective route for the commercialization of fuel cells.

1.5 References

[1] Murray, C. B.; Norris, D. J.; Bawendi, M. G. *J. Am. Chem. Soc.* **1993**, *115* (19), 8706–8715.

[2] Wang, Y.-J.; Zhao, N.; Fang, B.; Li, H.; Bi, X. T.; Wang, H. *Chem. Rev.* **2015**, *115* (9), 3433–3467.

[3] Min, Y.; Caster, J. M.; Eblan, M. J.; Wang, A. Z. *Chem. Rev.* **2015**, *115* (19), 11147–11190.

[4] Cuenya, B. R. *Thin Solid Films* **2010**, *518* (12), 3127–3150.

[5] Holby, E. F.; Sheng, W.; Shao-Horn, Y.; Morgan, D. *Energy Environ. Sci.* **2009**, *2* (8), 865.

[6] Shiju, N. R.; Alberts, A. H.; Khalid, S.; Brown, D. R.; Rothenberg, G. *Angew. Chem. Int. ed.* **2011**, *50* (41), 9615–9619.

[7] Lee, J. E.; Lee, N.; Kim, T.; Kim, J.; Hyeon, T. *Acc. Chem. Res.* **2011**, *44* (10), 893–902.

[8] Lu, A.-H.; Salabas, E. L.; Schüth, F. *Angew. Chem. Int. ed.* **2007**, *46* (8), 1222–1244.

[9] Liang, H.-W.; Brüller, S.; Dong, R.; Zhang, J.; Feng, X.; Müllen,

K. *Nat. Commun.* **2015**, *6*, 7992.

[10] Lu, A.-H.; Salabas, E. L.; Schüth, F. *Angew. Chem. Int. ed.* **2007**, *46* (8), 1222–1244.

[11] Datta, A.; Ebert, K.; Plenio, H. *Organometallics* **2003**, *22* (23), 4685–4691.

[12] Liu, J.; Qiao, S. Z.; Hu, Q. H.; Lu, G. Q. M. *Small* **2011**, *7* (4), 425–443.

[13] Lu, A.; Schmidt, W.; Matoussevitch, N.; Bönnemann, H.; Spliethoff, B.; Tesche, B.; Bill, E.; Kiefer, W.; Schüth, F. *Angew. Chem. Int. Ed.* **2004**, *116* (33), 4403–4406.

[14] Thomas, J. M.; Raja, R.; Lewis, D. W. Angew. Chem. Int. ed. 2005, 44 (40), 6456–6482.

[15] Gelman, F.; Blum, J.; Avnir, D. *Angew. Chem. Int. ed.* **2001**, *113* (19), 3647–3649.

[16] Shang, F.; Sun, J.; Wu, S.; Liu, H.; Guan, J.; Kan, Q. *J. Colloid Interface Sci.* **2011**, *355* (1), 190–197.

[17] Huang, Y.; Trewyn, B. G.; Chen, H.-T.; Lin, V. S.-Y. *New J.*

Chem. **2008**, *32* (8), 1311-1313.

[18] Yang, Y.; Liu, X.; Li, X.; Zhao, J.; Bai, S.; Liu, J.; Yang, Q. *Angew. Chem. Int. Ed.* **2012**, *51* (36), 9164–9168.

[19] Shylesh, S.; Wagner, A.; Seifert, A.; Ernst, S.; Thiel, W. R. Chem. Eur. J. **2009**, *15* (29), 7052–7062.

[20] Margelefsky, E. L.; Zeidan, R. K.; Davis, M. E. *Chem. Soc. Rev.* **2008**, *37* (6), 1118–1126.

[21] Shang, F.; Sun, J.; Wu, S.; Liu, H.; Guan, J.; Kan, Q. *J. Colloid Interface Sci.* **2011**, *355* (1), 190–197.

[22] Bass, J. D.; Solovyov, A.; Pascall, A. J.; Katz, A. *J. Am. Chem. Soc.* **2006**, *128* (11), 3737–3747.

[23] Tang, H.; Qi, Z.; Ramani, M.; Elter, J. F. *J. Power Sources* **2006**, *158* (2 SPEC. ISS.), 1306–1312.

[24] Meier, J. C.; Galeano, C.; Katsounaros, I.; Witte, J.; Bongard, H. J.; Topalov, A. A.; Baldizzone, C.; Mezzavilla, S.; Schüth, F.; Mayrhofer, K. J. J. *Beilstein J. Nanotechnol.* **2014**, *5* (1), 44–67.

[25] Guo, L.; Jiang, W. J.; Zhang, Y.; Hu, J. S.; Wei, Z. D.; Wan, L. J.

ACS Catal. **2015**, *5* (5), 2903–2909.

[26] Pylypenko, S.; Borisevich, A.; More, K. L.; Corpuz, A. R.; Holme, T.; Dameron, A. a.; Olson, T. S.; Dinh, H. N.; Gennett, T.; O'Hayre, R. *Energy Environ. Sci* **2013**, *6* (10), 2957-2964.

Chapter 2. One-Pot Synthesis of Magnetically Recyclable Mesoporous Silica Supported Acid-Base Catalyst for Tandem Reactions

2.1 Introduction

Magnetic mesoporous nanocomposite materials have attracted tremendous scientific and technological interest because magnetic characteristics can be incorporated in mesoporous structures with large pore volume, high surface area, and easy functionalization capability.[1] Such nanocomposite materials have been extensively applied in various biomedical areas,[2] including separation of biomolecules,[3] magnetically guided targeted delivery,[4] and theragnostics.[5] Magnetic mesoporous nanocomposite materials immobilized with catalytic species have also been extensively investigated as magnetically recyclable catalysts for organic reactions.[6] General synthesis of the magnetic mesoporous materials requires extra work to synthesize and purify the uniform sized magnetic nanoparticles beforehand. In otherwise, the

method involves high temperature process or strong chemical environments to form magnetic species on the surface of the mesoporous materials. Despite of their many potential applications, one-step synthesis of the magnetic mesoporous functional materials has been rarely proposed. [7]

Acid-base site-isolated catalysts, which were inspired by enzymes that can effectively perform multistep catalytic reactions through cooperative interactions of isolated catalytic active sites, have been intensively investigated as single-site heterogeneous catalysts.[8] Several silica nanostructured materials have been employed as heterogeneous supports[9] for the site-isolated immobilization of acidic and basic catalytic species,[10] and many research groups have tried to improve the catalytic performance by controlling the morphology[11] and structure of the catalysts.[12] Herein, we report a facile one-pot synthesis of a magnetically recyclable mesoporous silica catalyst for acid-base tandem reactions. We also present results of the effect of pore size on the catalytic activity of the mesoporous materials.

2.2 Experimental Section

2.2.1 Chemicals

iron(II) chloride tetrahydrate, iron(III) chloride hexahydrate, cethyltrimethylammonium bromide (CTAB), sodium hydroxide, tetraethylorthosilicate (TEOS), mesitylene, ethyl acetate, 2-(4-chlorosulfonylphenyl)ethyltrimethoxysilane (CESE) dissolved in dichloromethane, and [3-(2-aminoethylamino)propyl]trimethoxysilane (AAPS) were purchased from Sigma-Aldrich. All reagents were used without further purification.

2.2.2 Synthesis of Magnetically Separable Mesoporous Silica Acid-Base Site Isolated Catalyst

In typical synthesis, 0.1 g of iron(II) chloride tetrahydrate, 0.27 g of iron(III) chloride hexahydrate and 0.1 g of cethyltrimethylammonium bromide (CTAB) were dissolved in distilled water. This solution was stirred for 5 min at 70 ^{o}C, and 4 mL of 2 M sodium hydroxide aqueous

solution was rapidly injected. 0.5 mL of tetraethylorthosilicate (TEOS) and mesitylene was slowly added, followed by addition of 0.5 mL of ethyl acetate to the solution. Subsequently, 2-(4-chlorosulfonylphenyl) ethyltrimethoxysilane dissolved in dichloromethane (CESE, 100 μL) and [3-(2-aminoethylamino)propyl]trimethoxysilane (AAPS, 100 μL) was added with vigorous stirring, and this solution was aged for 6 h. The resulting MMAB catalyst was obtained by introducing the mixture of hydrochloric acid (40 μL) and ethanol (20 mL) solution at 60 ^{o}C for 3 h to remove CTAB and to activate sulfonic acid functional groups.

2.2.3 Characterization

Transmission electron microscopy (TEM) analysis was performed using a JEOL JEM-2100F (Jeol). X-ray diffraction (XRD) was measured by a D/Max-3C diffractometer (Rigaku) equipped with a rotating anode and a Cu *K*α radiation source (λ = 0.15418 nm), The magnetic properties were characterized using a vibrating sample magnetometer (Quantum Design PPMS VSM). Nitrogen adsorption-desorption isotherm by a 3FLEX surface characterization analyzer (Micromeritics). Fourier

transform infrared (FT-IR) spectra were obtained on a Perkin Elmer Spectrum One FT-IR spectrophotometer using KBr pellets. Reaction products were analyzed by Agilent 9575 (GC-MS), and thermogravimetric analysis (TGA) was carried out on a thermal analyzer (Perkin Elmer TAC 7/DX). Inductively-coupled plasma-atomic emission spectra (ICP-AES) were measured using Shimadzu ICPS-1000 IV ICP-AES spectrometer.

2.2.4 Catalytic Performance Test for Deacetalization-Henry Tandem Reaction

1mmol of benzaldehyde dimethyl acetal, 5mL of nitromethane, and 30 mg of catalyst were placed in a round-bottom flask, which was backfilled with argon. The reaction mixture was heated up to 90 ^{o}C, and maintained at this temperature for 5 hr with vgrous stirring. After the reaction termination, the reaction mixture was cooled down to room temperature and the catalyst was separated using a magnet. The separated catalyst was reused for subsequent reactions without regeneration or further addition of the catalyst for the recycle test.

2.3 Result and Discussion

2.3.1 Synthesis of the Magnetically Separable Mesoporous Silica Support and Acid-Base Catalyst Functionalization

We synthesized magnetic mesoporous silica nanocomposite materials by combining the Massart method[13] for magnetite nanoparticles and the previously reported synthetic procedure for mesoporous acid-base catalyst.[14] First, iron(II) chloride tetrahydrate, iron(III) chloride hexahydrate, and cetyltrimethylammonium bromide (CTAB) were dissolved in distilled water. This solution was stirred for 5 min at 70 °C, and 2 M aqueous sodium hydroxide was rapidly added. The color of the solution immediately changed from light yellow to black, indicating the formation of the magnetite nanoparticles upon reaction with hydroxide ions. Without any purification or drying, tetraethyl orthosilicate (TEOS) and a swelling agent, mesitylene, were slowly added to the resulting solution, followed by addition of ethyl acetate. Subsequently, 2-(4-chlorosulfonylphenyl)ethyltr-imethoxysilane (CESE) dissolved in dichloromethane and [3-(2-aminoethylamino)propyl]trimethoxysilane

(AAPS) were added with vigorous stirring, and the resulting mixture was aged for 6 h at 70 °C. Because of the presence of residual hydroxide ions after the magnetite synthesis, addition of extra aqueous sodium hydroxide was not necessary to accelerate the condensation of the silanol groups. The powdery product was retrieved by centrifugation, and was further treated with a mixture of hydrochloric acid and ethanol to remove CTAB and to activate the sulfonic acid groups, thereby producing the final magnetic mesoporous silica nanocomposite with immobilized acidic (sulfonic acid) and basic (diamine) groups.

TEM images of the synthesized nanocomposite materials revealed that ~ 9 nm Fe_3O_4 nanoparticles were enveloped by mesoporous silica shells (**Figure 2.1**). The average pore size and surface area were found to be 5.4 nm and 327 m^2/g, respectively, and the material is designated as MMAB (**Figure 2.2**). When we performed the synthesis without using the swelling agent (mesitylene), mesoporous material with a pore size of 2.4 nm and a surface area of 285 m^2/g was generated (designated as MMAB-SP). The X-ray diffraction (XRD) pattern revealed that the embedded iron oxide nanoparticles were magnetite, Fe_3O_4 (**Figure** 2.3). The synthesized nanocomposite showed superparamagnetic

characteristics with high saturation magnetization of 78 emu/g of Fe at 300 K (**Figure 2.4 and 2.5**). This superparamagnetic property is advantageous for the efficient recycling of catalysts because the residual magnetic moment in ferromagnetic materials prevents rapid redispersion.[15] For the catalyst characterization, we performed Fourier-transform infrared spectroscopy (FT-IR) and X-ray photoelectron Spectroscopy (XPS) analysis of MMAB (**Figure 2.6 and 2.7**), and we confirmed the amine and sulfonic acid moieties were properly loaded on the magnetic mesoporous material. Furthermore, we confirmed that both acid and base functions were properly working in the catalysts by monitoring NH3 and CO2 temperature programed desorption (NH3-TPD, CO2-TPD) profiles (**Figure 2.8 and 2.9**).

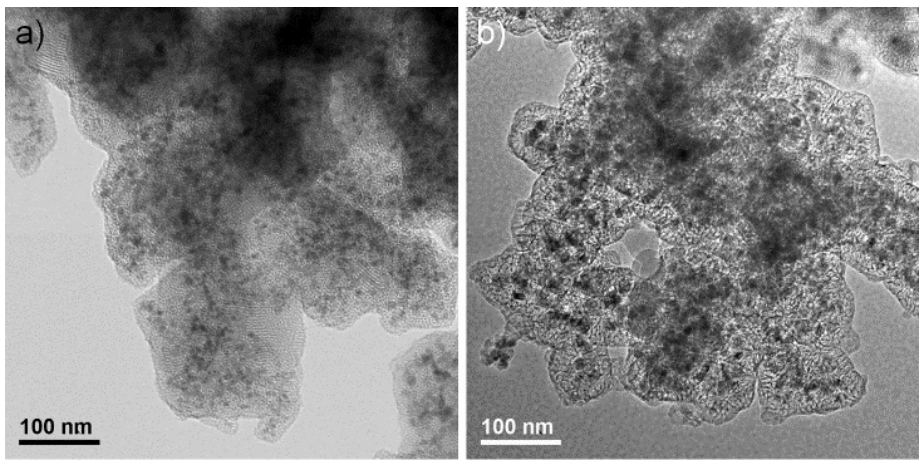

Figure. 2.1. TEM images of the magnetic mesoporous acid-base catalyst prepared (a) without a swelling agent and (b) with a swelling agent.

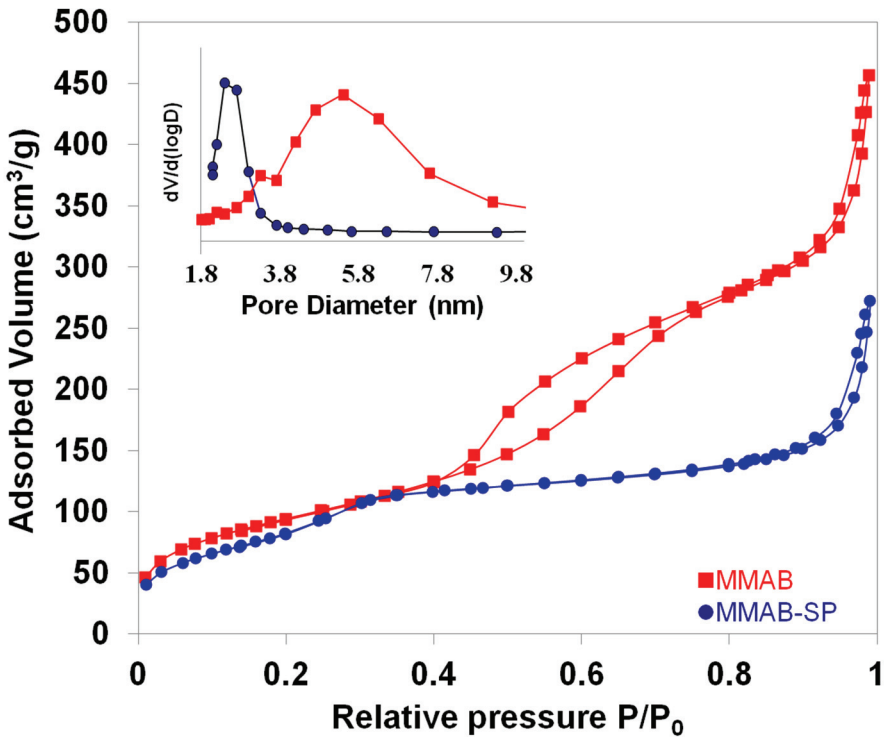

Figure. 2.2. The N_2 adsorption-desorption isotherms and corresponding pore size distributions of the catalysts with large pore size (MMAB) and small pore size (MMAB-SP).

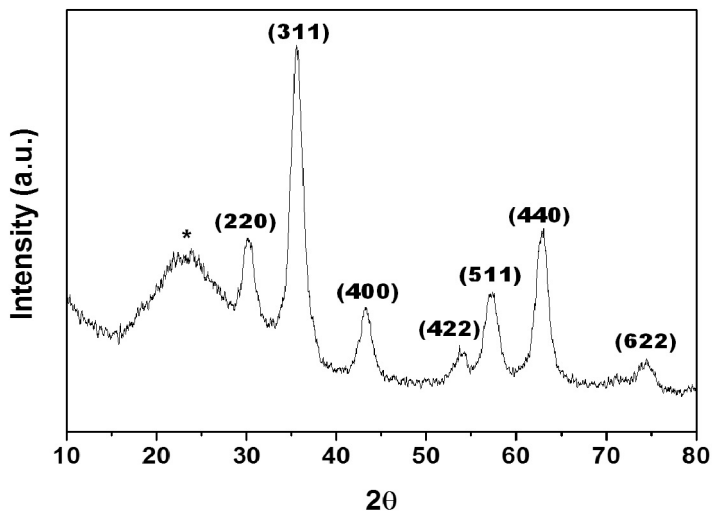

Figure 2.3. The powder X-ray diffraction (XRD) pattern of the synthesized catalyst (PDF#: 99-0073). Diffusive peak from 20^{o} to 30^{o} is due to amorphous silica part in the material

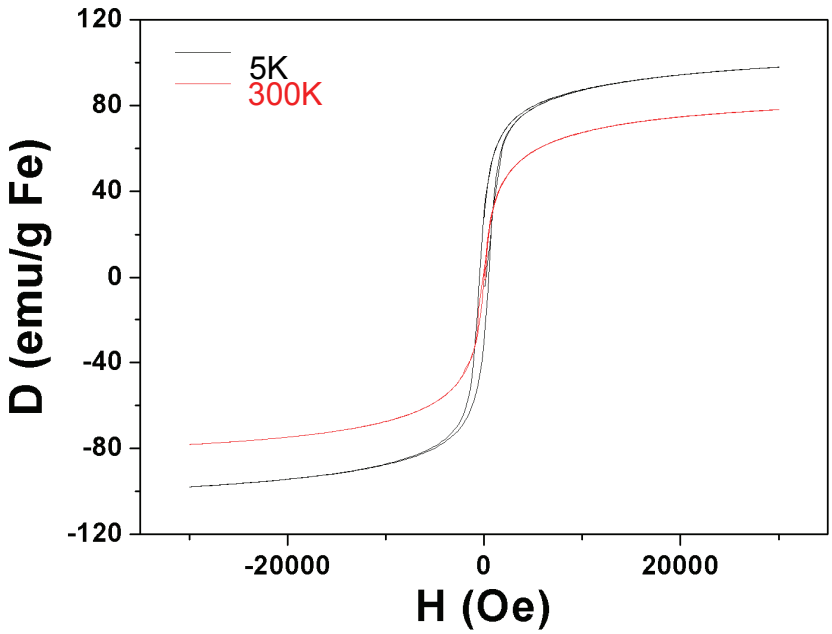

Figure 2.4. Magnetic behavior of MMAB measured at 5 K and 300 K.

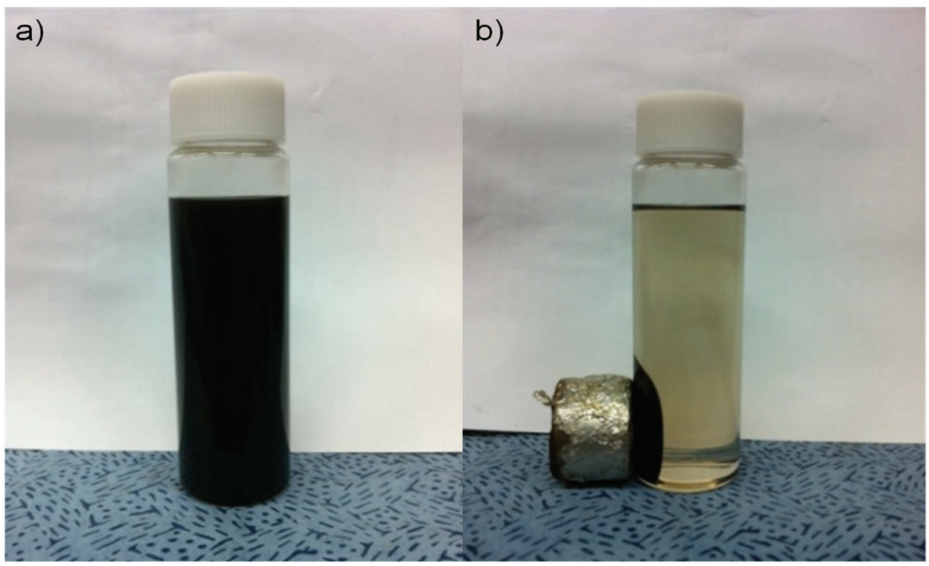

Figure 2.5. Magnetic separation of the synthesized MMAB catalyst; (a) dispersed in nitromethane and (b) in the presence of magnetic force.

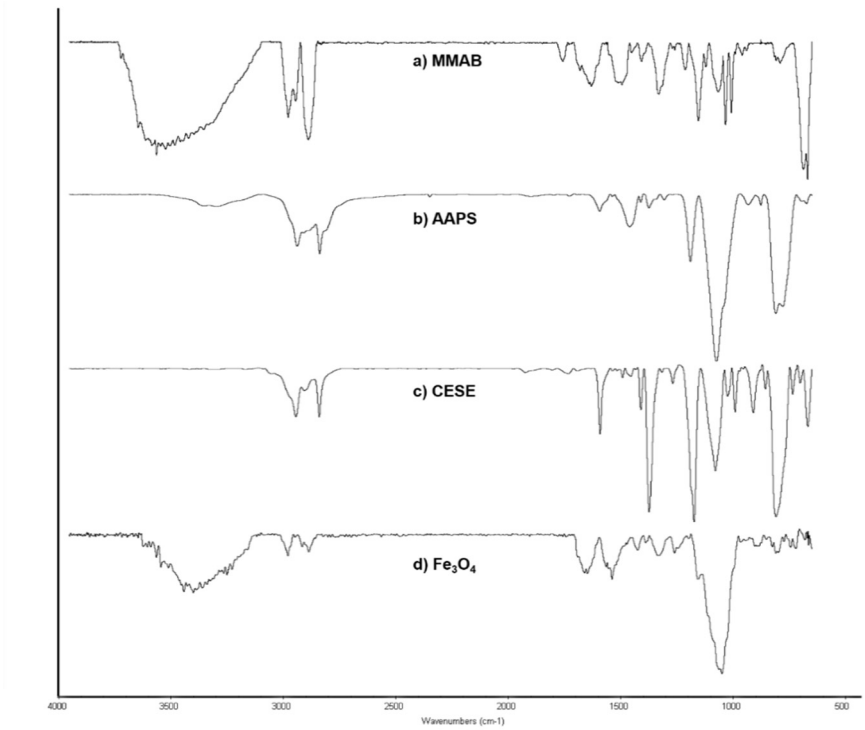

Figure 2.6. FT-IR spectra of (a) MMAB, (b) AAPS, (c) CESE, and (d) Fe_3O_4

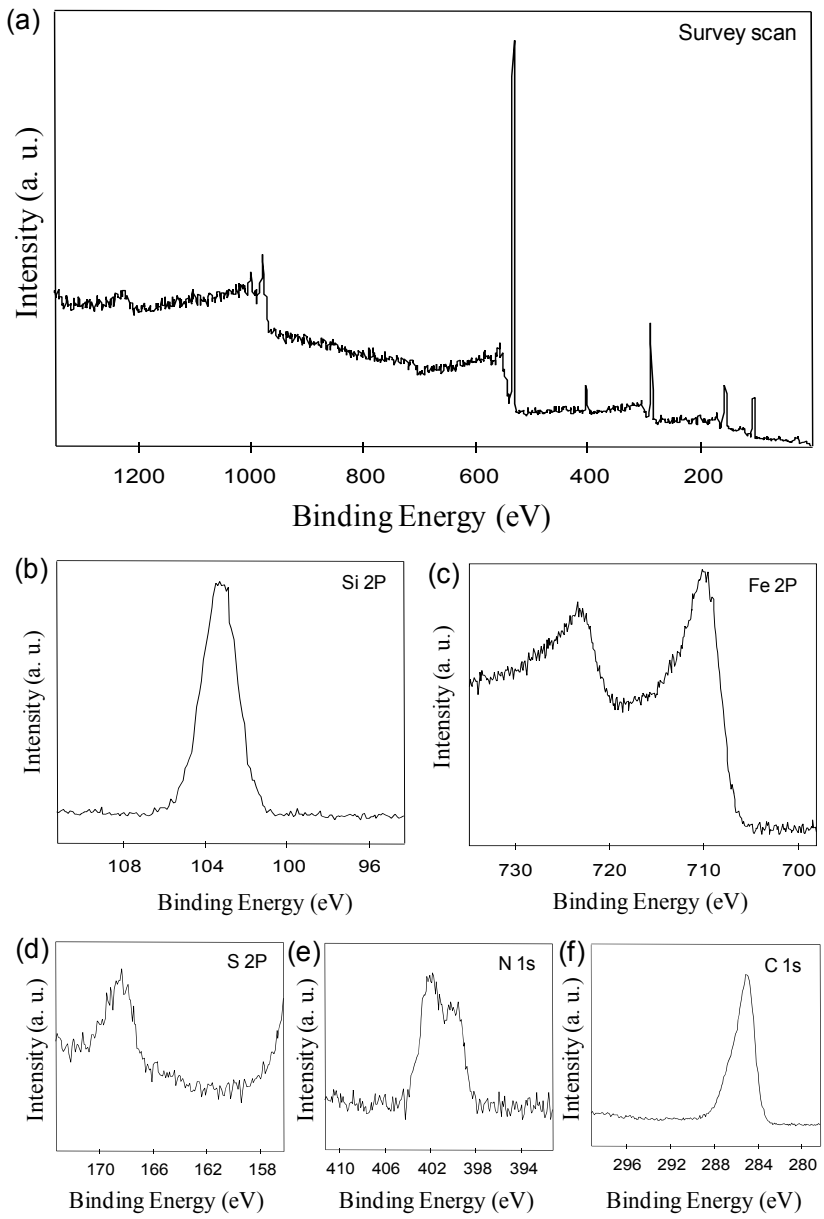

Figure. 2.7. XPS spectra of MMAB: (a) survey scan; high resolution scans of (b) Si 2p, (c) Fe 2p, (d) S 2p, (e) N 1s and (e) C 1s.

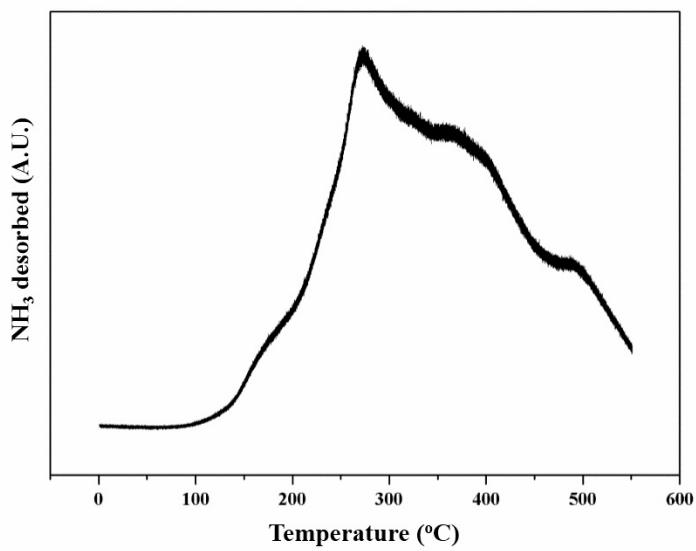

Figure 2.8. NH_3-TPD profile of MMAB

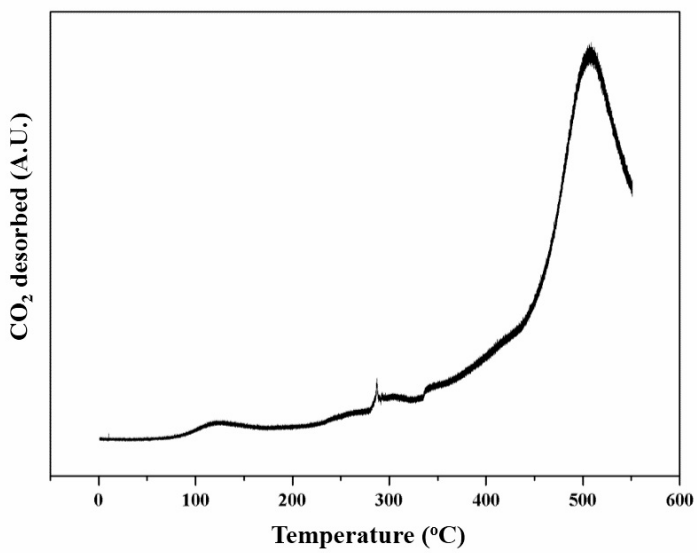

Figure 2.9. CO_2-TPD profile of MMAB

2.3.2 Catalytic Performance Test for Deacetalyzation-Henry Tandem Reaction

To examine the catalytic activity of MMAB, we performed a one-pot tandem reaction that converts benzaldehyde dimethyl acetal (1) to benzaldehyde (2) via acid-catalyzed deacetalization, followed by conversion of 2 to 1-nitro-2-phenylethylene (3) via the base-catalyzed Henry reaction (**Scheme 2.1, Table 2.1**). The catalyst showed excellent performance with very high yield and selectivity (entry 1 of **Table 2.1**), and as expected, the reaction did not proceed without the catalyst (entry 2 of **Table 2.1**). Comparative catalytic reactions were conducted to demonstrate the importance of both the acidic and basic functional groups. When the magnetic mesoporous silica catalyst with only basic groups (MMB) was used, the reaction did not proceed owing to the absence of the acid catalyzed deacetalization reaction that converts benzaldehyde dimethyl acetal to benzaldehyde (entry 3 of **Table 2.1**). However, when benzaldehyde was used as a starting material, 1-nitro-2-phenylethylene was produced nearly quantitatively (entry 4 of **Table 2.1**). Meanwhile, the catalyst derivatized only with acidic groups (MMA) did

transform benzaldehyde dimethyl acetal to benzaldehyde, but could not catalyze the final reaction to form 1-nitro-2-phenylethylene (entry 5 of **Table 2.1**).

Catalyst lifetime and recyclability are very important for large-scale industrial applications. The MMAB catalyst showed excellent recyclability, maintaining high activity for up to five runs (**Table 2.2**). In addition, MMAB could be easily recovered using a magnet after each reaction, and could be reused for subsequent reactions without regeneration or further addition of catalyst.

Next, we compared the catalytic activities of mesoporous silica catalysts with different pore sizes. We ran the catalytic reactions with the 5.4 nm MMAB and 2.4 nm MMAB-SP under identical reaction conditions, and aliquots were drawn from the reaction mixtures at 15 min intervals. The yield of product 3 in each sample was measured and the results are shown in **Figure 2.10**. With MMAB, the reaction was completed within 4.5 h, while the reaction with MMAB-SP took more than 7 h for the completion. This dramatic increase of reaction rate for the larger pore-sized silica materials can be explained by internal pore diffusion.[16,17] Internal pore diffusivity, which is a function of Knudsen diffusivity, is known to

increase as pore sizes increase for diffusion-controlled reactions.[16] Because we synthesized MMAB and MMAB-SP using nearly identical procedures with a similar loading of the catalytic functional groups (**Table 2.3**), the different catalytic activity can be explained solely by the difference in pore size.

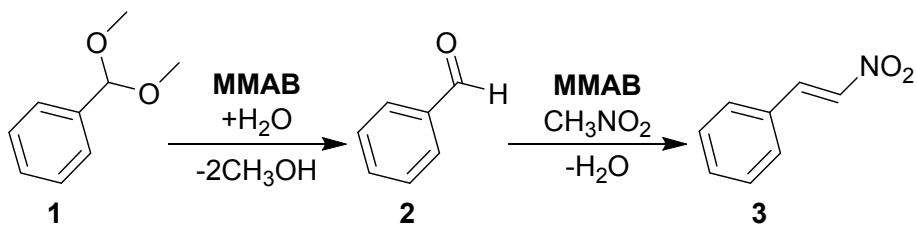

Scheme 2.1. Conversion of benzaldehyde dimethyl acetal (1) to 1-nitro-2-phenylethyelene (3) by MMAB catalysis. Benzaldehyde (2) is the intermediate of the tandem reaction.

Entry	Catalyst	Reactant	Product	Yield (%)
1	MMAB	**1**	**2** and **3**	2 (**2**)/96 (**3**)
2	N/A	**1**	—	—
3	MMB	**1**	—	—
4	MMB	**2**	**3**	98
5	MMA	**1**	**2**	93

Table 2.1. Catalytic deacetalization and Henry reaction using various magnetic mesoporous materials[a]

[a] Reaction conditions: benzaldehyde dimethyl acetal (1 mmol), nitromethane (5 mL), catalyst (30 mg). 90 °C, 5 h.

Cycle	1st	2nd	3rd	4th	5th
Yield (%)	95	94	93	91	91

Table 2.2. Magnetic separation and recycling results for the MMAB catalyst in the tandem reaction of 1 to yield 3[a]

[a] Reaction conditions: benzaldehyde dimethyl acetal (1 mmol), nitromethane (5 mL), MMAB nanocatalyst (30 mg). 90 °C, 5 h.

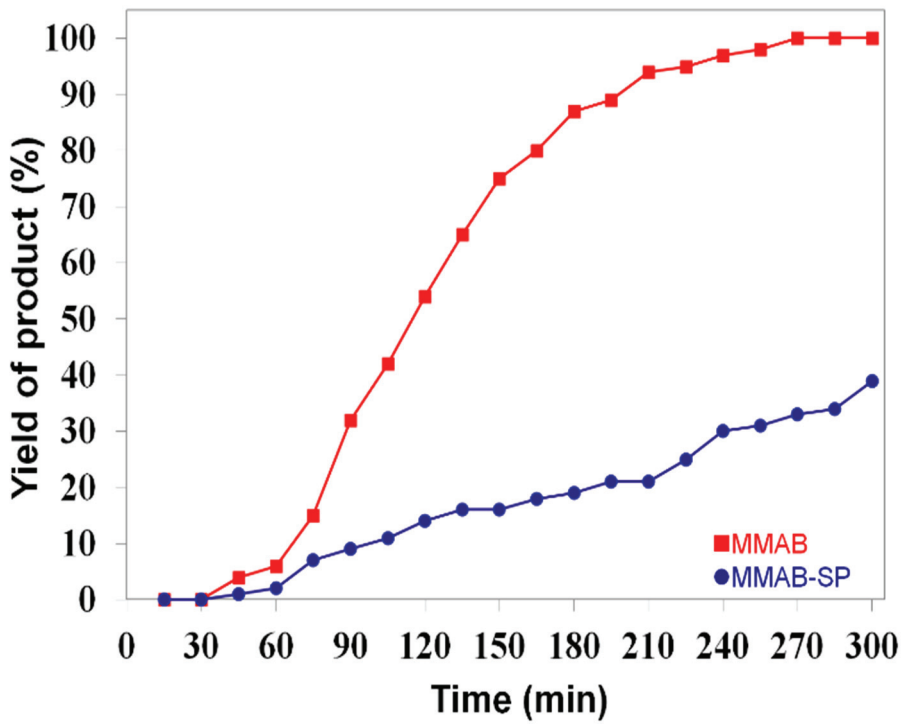

Figure 2.10. Time-dependent product yield of the tandem deacetalization-Henry reaction using MMAB and MMAB-SP catalysts. Reaction conditions: benzaldehyde dimethyl acetal (1 mmol), nitromethane (5 mL), MMAB (30 mg) or MMAB-SP (30 mg), 90 °C, 5 h.

Sample	Elemental Contents (wt %)			
	C	H	N	S
MMAB	15.85	3.313	1.744	2.256
MMAB-SP	15.28	3.638	1.726	2.281

Table 2.3. The CHNS elemental analysis results of MMAB and MMAB-SP.

2.4 Conclusion

In conclusion, we have successfully synthesized a magnetically separable mesoporous site-isolated acid-base catalyst using a one-pot reaction. The catalyst showed excellent performance with very high yield and selectivity for the conversion of benzaldehyde dimethyl acetal to 1-nitro-2-phenylethylene via benzaldehyde using tandem acid-catalyzed deacetalization and base-catalyzed Henry reaction. The catalyst could be easily recovered by using a magnet and dispersed in subsequent reaction mixtures, enabling recycling of the catalyst for up to five uses without losing catalytic activity. Furthermore, comparative studies revealed that the larger-pore-sized materials exhibited higher catalytic activity than the smaller-pore-sized materials. We believe that the current synthetic approach for this magnetic mesoporous acid-base site-isolated catalyst will contribute to the practical applications of tandem catalysts.

2.5 References

[1]. (a) J. Liu, S. Z. Qiao, Q. H. Hu, and G. Q. M. Lu, Small, 2011, 7, 425; (b) A.-H. Lu, E. L. Salabas, and F. Schüth, Angew. Chem., Int. ed., 2007, 46, 1222.

[2]. (a) K. M. L. Taylor-Pashow, J. Della Rocca, R. C. Huxford, and W. Lin, Chem. Commun., 2010, 46, 5832; (b) J. Liu, S. Z. Qiao, J. S. Chen, X. W. Lou, X. Xing, and G. Q. Lu, Chem. Commun., 2011, 47, 12578.

[3]. (a) T. Sen, A. Sebastianelli, and I. J. Bruce, J. Am. Chem. Soc., 2006, 128, 7130; (b) Y. Deng, D. Qi, C. Deng, X. Zhang, and D. Zhao, J. Am. Chem. Soc., 2008, 130, 28.

[4]. (a) J. Kim, H. S. Kim, N. Lee, T. Kim, H. Kim, T. Yu, I. C. Song, W. K. Moon, and T. Hyeon, Angew. Chem., Int. ed., 2008, 47, 8438; (b) W. Zhao, J. Gu, L. Zhang, H. Chen, and J. Shi, J. Am. Chem. Soc., 2005, 127, 8916; (c) W. Zhao, H. Chen, Y. Li, L. Li, M. Lang, and J. Shi, Adv. Funct. Mater., 2008, 18, 2780.

[5]. (a) M. W. Ambrogio, C. R. Thomas, Y.-L. Zhao, J. I. Zink, and J. F. Stoddart, Acc. Chem. Res., 2011, 44, 903; (b) J. E. Lee, N.

Lee, T. Kim, J. Kim, and T. Hyeon, Acc. Chem. Res., 2011, 44, 893; (c) S. Giri, B. G. Trewyn, M. P. Stellmaker, and V. S.-Y. Lin, Angew. Chem., Int. ed., 2005, 44, 5038; (d) J. E. Lee, N. Lee, H. Kim, J. Kim, S. H. Choi, J. H. Kim, T. Kim, I. C. Song, S. P. Park, W. K. Moon, and T. Hyeon, J. Am. Chem. Soc., 2010, 132, 552.

[6]. (a) A.-H. Lu, W. Schmidt, N. Matoussevitch, H. Bönnemann, B. Spliethoff, B. Tesche, E. Bill, W. Kiefer, and F. Schüth, Angew. Chem., Int. Ed., 2004, 116, 4403; (b) M. Shokouhimehr, Y. Piao, J. Kim, Y. Jang, and T. Hyeon, Angew. Chem., Int. ed., 2007, 46, 7039.

[7]. L. Han, H. Wei, B. Tu, and D. Zhao, Chem. Commun., 2011, 47, 8536.

[8]. (a) J. M. Thomas, R. Raja, and D. W. Lewis, Angew. Chem., Int. ed., 2005, 44, 6456; (b) F. Gelman, J. Blum, and D. Avnir, Angew. Chem., Int. Ed., 2001, 40, 3647.

[9]. (a) B. Kesanli and W. Lin, Chem. Commun., 2004, 2284; (b) C. Perego and R. Millini, Chem. Soc. Rev., 2013,42, 3956.

[10]. (a) E. L. Margelefsky, R. K. Zeidan, and M. E. Davis, Chem. Soc. Rev., 2008, 37, 1118; (b) N. R. Shiju, A. H. Alberts, S. Khalid, D. R. Brown, and G. Rothenberg, Angew. Chem., Int. Ed., 2011, 50, 9615.

[11]. (a) L. Zhang, Y. Guo, J. Peng, X. Liu, P. Yuan, Q. Yang, and C. Li, Chem. Commun., 2011, 47, 4087; (b) Y. Li, H. Xia, F. Fan, Z. Feng, R. a. van Santen, E. J. M. Hensen, and C. Li, Chem. Commun., 2008, 774; (c) Y. Yang, X. Liu, X. Li, J. Zhao, S. Bai, J. Liu, and Q. Yang, Angew. Chem. Int. ed., 2012, 51, 9164.

[12]. (a) K. K. Sharma, A. Anan, R. P. Buckley, W. Ouellette, and T. Asefa, J. Am. Chem. Soc., 2008, 130, 218; (b) J. D. Bass, A. Solovyov, A. J. Pascall, and A. Katz, J. Am. Chem. Soc., 2006, 128, 3737; (c) K. Motokura, N. Fujita, K. Mori, T. Mizugaki, K. Ebitani, and K. Kaneda, J. Am. Chem. Soc., 2005, 127, 9674; (d) F. Shang, J. Sun, S. Wu, H. Liu, J. Guan, and Q. Kan, J. Coll. Int. Sci., 2011, 355, 190.

[13]. Massart, R. IEEE Trans. Magn., 1981, 17, 1247.

[14]. (a) R. Zeidan, V. Dufaud, and M. Davis, J. Catal., 2006, 239,

299; (b) S. Shylesh, A. Wagner, A. Seifert, S. Ernst, and W. R. Thiel, Chem. Eur. J., 2009, 15, 7052.

[15]. C. T. Yavuz, J. T. Mayo, W. W. Yu, A. Prakash, J. C. Falkner, S. Yean, L. Cong, H. J. Shipley, A. Kan, M. Tomson, D. Natelson, and V. L. Colvin, Science, 2006, 314, 964.

[16]. (a) M. Shimura, Y. Shiroto, and C. Takeuchi, Ind. Eng. Chem. Fundam., 1986, 25, 330; (b) H. Takahashi, B. Li, T. Sasaki, C. Miyazaki, T. Kajino, and S. Inagaki, Chem. Mater., 2000, 12, 3301; (c) M. Iwamoto, Y. Tanaka, N. Sawamura, and S. Namba, J. Am. Chem. Soc., 2003, 125, 13032.

[17]. (a) J. T. Richardson, Principles of Catalyst Development; Plenum Press: New York, 1989; (b) H. S. Fogler, Elements of Chemical Reaction Engineering, 3rd ed.; Prentice-Hall: New Jersey, 1999.

Chapter 3. Highly Durable and Active PtFe Nanocatalyst for Electrochemical Oxygen Reduction Reaction

3.1 Introduction

Nanoparticle-based electrocatalysts have been intensively investigated for fuel cell applications over the last decade, mainly motivated by their high mass activity.[1-14] Many research groups have made great effort to utilize the high activity and surface area of nanoparticles (NPs) in order to make a breakthrough for fuel cell commercialization. However, practical use of nanomaterials for fuel cell electrocatalyst was impeded by their low physical and chemical stability. Under the standard fuel cell operating conditions, NPs are often oxidized, dissolved, or detached from the support and agglomerated into larger particles, losing their electrochemical catalytic activity during cycling.[15] Moreover, according to theoretical calculations, the oxidation and dissolution potentials of NPs tend to decrease with their sizes.[16] In these regards,

ordered intermetallic NPs are considered as one of the most promising candidates to achieve both high activity and stability in the practical fuel cell applications.[17-23] The Sun group reported that the ordered intermetallic PtFe NPs of face-centered tetragonal (fct) structure have superior iron anti-dissolution property under the acidic fuel cell operating condition. In addition, fct-PtFe NPs show higher activity than the disordered face-centered cubic (fcc) PtFe NPs.[17] The Abruna group reported the superior long-term stability of ordered fct-PtCo NPs,[18] which is attributed to the Pt-rich surface and the strong Pt-Co bonding in the core of the NPs. Despite of these advantages, however, the synthesis of small-sized ordered fct-PtFe NPs with high mass activity has been rarely reported so far. In general, as-synthesized PtFe NPs have disordered fcc structure, and consequently thermal annealing at ~700 oC is necessary to transform them into ordered fct structure,[24] which inevitably leads to the coalescence of the NPs forming larger and polydisperse NPs. To prevent this coalescence during annealing, protective coating of the NPs with inorganic shells[17,25] or physical barriers[26] have been suggested. However, this approach requires additional step of removing the coating layer from the surface of the NPs

to expose the active sites, which increases time and cost in the production.

In the meantime, there has been another approach to utilize protective coating to enhance the long-term performance of fuel cells. By coating NPs deposited on the support with protective layer, they can be made more resistive toward detachment and agglomeration, which are the major deactivation mechanisms during the fuel cell operation, as mentioned above.[27] So far, various coating layers including carbon shell,[28] inorganic barrier,[29] and graphitic hallow spheres[30,31] are proposed, and the protective layer-coated NPs show better performance in terms of the long-term stability compared to the uncoated counterparts. Especially, it is known that N-doped carbon has very good affinity to the surface of metal NPs and, thus, stabilizes the small NPs not to agglomerate during the fuel cell operation.[32] However, it was criticized that, although with enhanced stability, the presence of protective layer can lower the catalytic performance by blocking the active sites and lowering the mass transport rate at the surface of the NPs.

Being inspired from those two different approaches to improve the long-term stability of nanocatalysts, we designed a nanoparticle-based electrocatalyst that combines those approaches together and overcomes

their limitations. Herein, we report a synthetic method of highly durable and active PtFe NPs with very thin "dual purpose" N-doped carbon shell. This carbon shell is *in situ* formed from polydopamine coating of disordered fcc-PtFe NPs during thermal annealing to transform the NPs into ordered fct structure. The carbon shell effectively prevents PtFe NPs from coalescence by the annealing so that fct-PtFe NPs as small as 6.5 nm can be obtained. Moreover, by controlling the thickness of the carbon shell in sub-nanometer scale, the shell also acts as highly effective protective coating of the NPs during fuel cell cycling while it is still permeable for the reactant molecules and not affecting their electrocatalytic activity. In half-cell and membrane electrode assembly (MEA) tests, our N-doped carbon-coated PtFe NPs show excellent long-term stability for realistic fuel cell application. The origin of the stability of our nanocatalyst is investigated with *in situ* synchrotron X-ray absorption spectroscopy, and the results confirm the critical importance of the ordered fct structure and the presence of N-doped carbon shell for the long term stability.

3.2 Experimental Section

3.2.1. Synthesis of PtFe Nanoparticles

0.2 g of $Pt(acac)_2$ (acac = acetylacetonate), 1.28 mL of oleic acid and 1.36 mL of oleylamine were stirred gently for 30 min at the room temperature under the Ar atmosphere. The temperature of mixture solution was increased to 120 ^oC, and 0.16 mL of $Fe(CO)_5$ was rapidly injected to the mixture solution. After the injection, the temperature of mixture solution was increased at the rate of 3 ^oC per minute until it reached to 220 ^oC, and kept at this temperature for 1 hr. After the reaction termination, the mixture solution was cooled down to room temperature and rinsed excessively with the mixture of 2-propanol and ethanol. After the washing process, PtFe NPs were dried in a vacuum oven for an hour.

3.2.2 Polydopamine Coating

Polydopamine coating was conducted by dopamine hydrochloride (Dopamine hydrochloride, Sigma Aldrich, 3 mg·ml-1) in tris-HCl buffer

solution (10 mM, pH 8.5 Tris-HCl (Trizma® base, Sigma Aldrich and hydrochloric acid, 37%, Sigma Aldrich 3 mg·ml-1).2 After treatment of the NPs with dopamine solution, the residual polydopamine was washed several times with ethanol and water. After drying the sample in vacuum oven (80 oC) overnight.

3.2.3 Thermal Annealing

After polydopamine coating, thermal annealing of the NPs was conducted at 700 oC 2 hr under 5 % H2+ Ar balanced to obtain ordered fct-PtFe/C. For comparison, disordered fcc-PtFe/C was prepared by thermal annealing at 400 oC for 2 hr under 99.99% Ar without polydopamine coating.

3.2.4 Characterization

Bright field and energy-filtered TEM images were obtained on a JEOL-2200FS equipped with an image Cs-corrector and an Omega filter. The HADDF-STEM and EDS measurements were performed on a JEM-

ARM200F and JEOL-2100F equipped with a Cs-corrector. All TEM instruments were operated at 200 kV. HRPD, HR-PES, and *in situ* XANES measurements were performed at Pohang Accelerator Laboratory (PAL) 9B beamline (λ = 1.4970 Å), 8A1 beamline ($h\nu$ = 630 eV), and 8C beamline. The details on the synchrotron X-ray measurements are provided in the Supporting Information.

3.2.5 Electrochemical Method

Electrochemical experiments were conducted in 0.1 M HClO4 at 293 K using a conventional three-compartment electrode system with an Autolab rotating disc electrode (RDE) and Autolab 302 potentiostat. A RDE electrode with 0.196 cm2 area glassy carbon electrode was used as working electrode. Saturated calomel electrode and Pt wire were used as reference and counter electrodes, respectively. All of the potentials are versus the reversible hydrogen electrode (RHE). Ink was prepared by mixing nanocatalyst, Nafion ionomer and 2-isopropanol. After sonication, ink was deposited onto the glassy carbon electrode and dried to form a uniform film. The Pt loading level was 7.8 μg gcm-2 in PtFe

alloy nanoparticles and 16.0 μgcm-2 in commercial Pt/C (Johnson Matthey Co., 20 wt %)

3.3 Result and Discussion

3.3.1 Preparation of Carbon Shell-Coated PtFe Nanocatalyst

The formation process of ordered fct-PtFe NPs with dual purpose N-doped carbon shell is illustrated in **Figure 3.1a**. Firstly, disordered fcc-PtFe NPs are synthesized via the previously reported method using platinum acetylacetonate [$Pt(acac)_2$] and iron pentacarbonyl [$Fe(CO)_5$] as Pt and Fe precursors, respectively (**Figure 3.2**).[33] As-synthesized PtFe NPs are supported on carbon particles and then coated with polydopamine by a treatment with dopamine hydrochloride solution. Thermal annealing of carbon-supported and dopamine-coated fcc-PtFe NPs at 700 ^{o}C leads to the formation of atomically ordered fct-PtFe NPs with N-doped carbon coating. The effect of *in situ* formed N-doped carbon shell is investigated by performing a control experiment without dopamine coating. As shown in **Figures 3.1b and 3.1c**, thermal annealing of carbon-supported PtFe NPs (PtFe/C) without dopamine coating leads to significant increase in the NP size up to tens of nanometers due to extensive coalescence. On the other hand, 6.5 nm-

sized NPs are obtained from thermal annealing of dopamine-coated PtFe/C, which is close to the initial size of the NPs before the annealing **(Figure 3.3**), which confirms that the *in situ* formed carbon shell makes the NPs highly resistive towards coalescence. Ordered intermetallic fct structure of PtFe/C after the annealing is confirmed by high resolution powder diffraction (HRPD) in Figure 1d in comparison with PtFe/C before annealing and pure Pt/C. The characteristic superlattice peaks of the ordered intermetallic fct structure appear after the annealing, as marked with asterisks. Also, high angle annular dark field-scanning transmission electron microscopy (HAADF-STEM) and fast Fourier transform (FFT) analysis (**Figures 3. 1e-1g**) confirm the ordered fct structure of PtFe NPs. In these images, the unit cell projected along [001] axis shows a periodic line array of Fe columns stacked by Pt columns.

Polydopamine is used as the precursor for *in situ* formation of N-doped carbon shell.[34] The thickness of N-doped carbon shell can be precisely controlled by the coating time of polydopamine.[35] TEM data show that the thickness of polydopamine coating is roughly proportional to the coating time (**Figure 3.4a**). In the case of 1 hr coating, the carbon shell with average thickness of ~ 0.43 nm is formed, which amounts

approximately two layers of carbon sheet (**Figure 3.5**). In high resolution photoemission spectroscopy (HR-PES) data, the presence of N-C and N-H bonding is confirmed in the N 1s signal from polydopamine-coated NPs before the annealing (**Figure 3.4b**). After thermal annealing at 700 °C, carbonization of dopamine takes place and signals from pyridinic (N 1s ~399 eV), pyrrolic (N 1s ~400 eV), and graphitic (N 1s ~401 eV) nitrogen are observed, indicating that dopamine is transformed into N-doped carbon shell. From a controlled sample without dopamine coating, no nitrogen signal is detected. The ratio of N 1s and Pt 4f signal intensities, which is proportional to the thickness of dopamine coating of PtFe NPs, is increased with the coating time (**Figure 3.6**), further supporting the result from the TEM data. Bright field and energy-filtered TEM (EF-TEM) images in **Figure 3.4c** and **Figure 3.7** reveal that nitrogen is mainly distributed in the carbon shell adjacent to the PtFe NP.

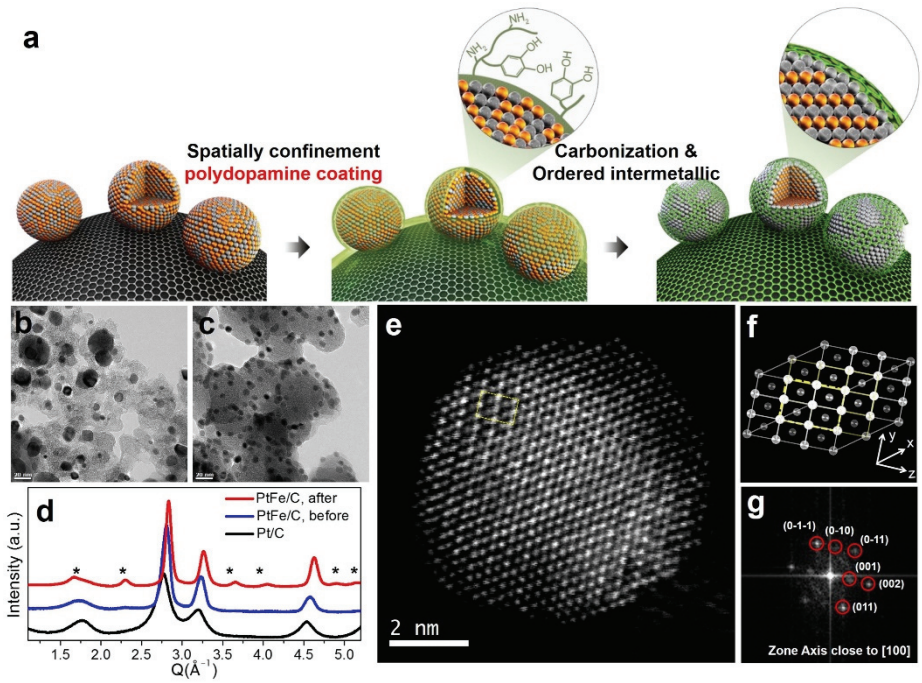

Figure 3.1. Synthesis of ordered intermetallic fct PtFe/C. (a) Schematic synthesis diagram of carbon-supported and N-doped carbon-coated ordered fct-PtFe NPs. (b-c) TEM images of thermally annealed NPs without (b) and with dopamine coating (c) at 700 °C. (d) HRPD data of carbon-supported pure Pt (Pt/C), PtFe NPs before annealing (PtFe/C, before), and after annealing (PtFe/C, after). (e-g) Cs-corrected HAADF-STEM image of a fct-PtFe NP after annealing (e), a model structure of fct-PtFe structure (f), and a FFT patterns of the image (g). The Pt columns look brighter than the Fe columns due to the Z-contrast.

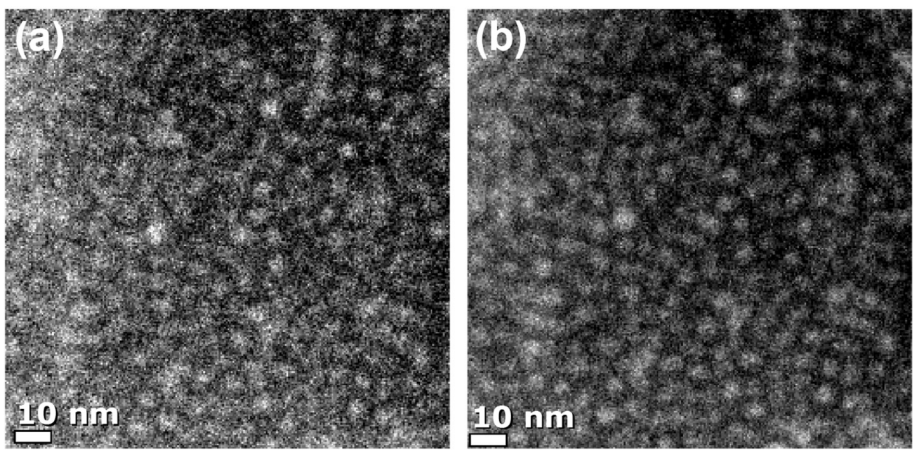

Figure 3.2. EF-TEM images of as-prepared PtFe nanoparticles (a) Pt and (b) Fe.

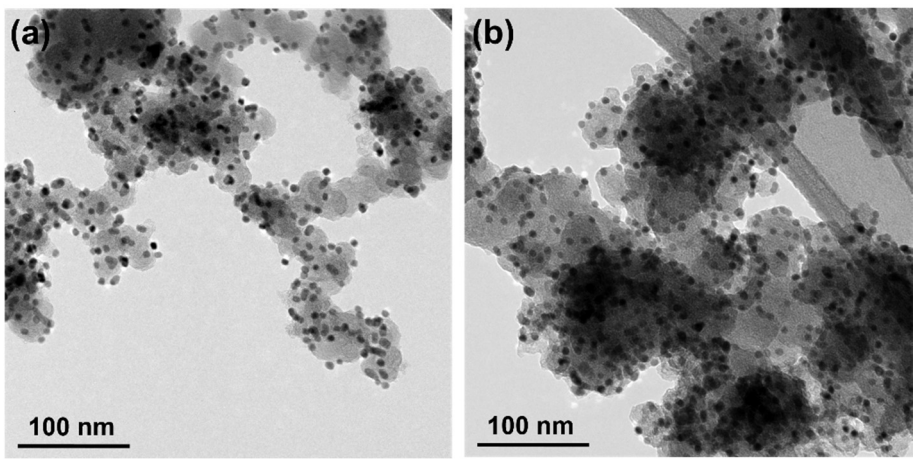

Figure 3.3. Low magnified TEM images of (a) as-prepared PtFe/C and (b) ordered fct-PtFe/C obtained by 1 hr dopamine coating and 700 ^{o}C annealing.

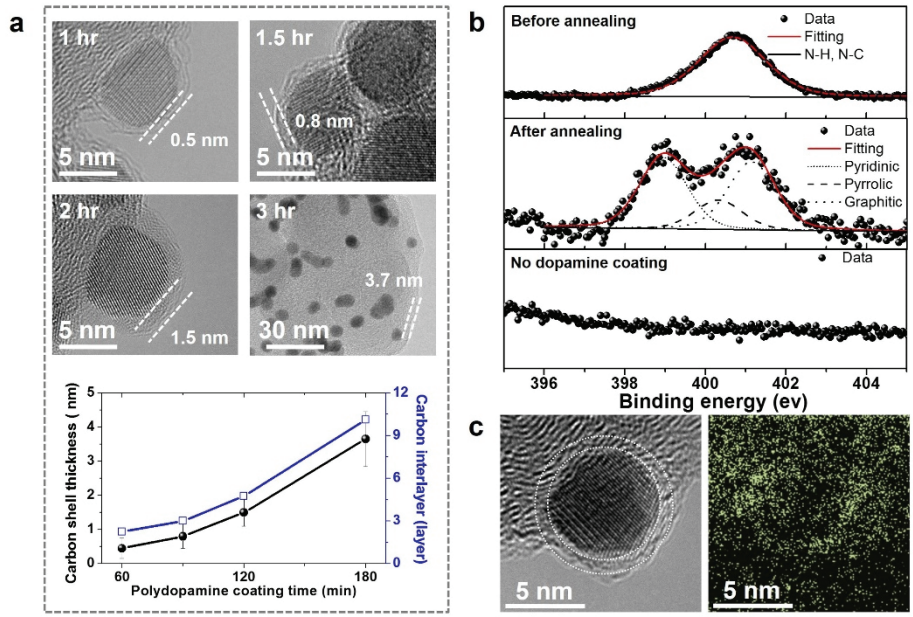

Figure 3.4. Characterizations of N-doped carbon shells. (a) TEM images of carbon-loaded and N-doped carbon shell-coated PtFe NPs and plots of the shell thickness (number of carbon interlayer) vs. polydopamine coating time. (b) HR-PES data around N 1s core level from PtFe NPs before annealing (top), after annealing, (middle), and without dopamine coating (bottom). (c) HR-TEM image of a carbon-supported and carbon shell-coated PtFe NP (left) and its EF-TEM image showing distribution of nitrogen (right).

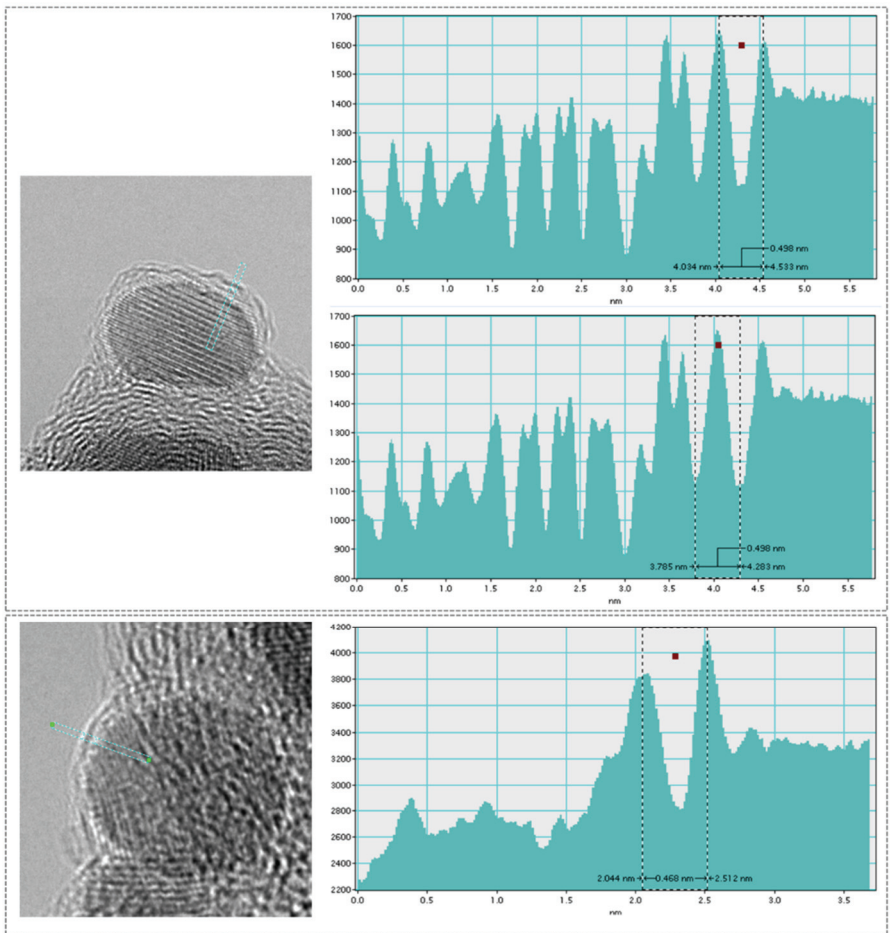

Figure 3.5.1. TEM analysis of the carbon-carbon interlayer distance. TEM images the samples with dopamine coating of 1 hr. The average thickness of each carbon layer is 0.43 ± 0.06 nm.

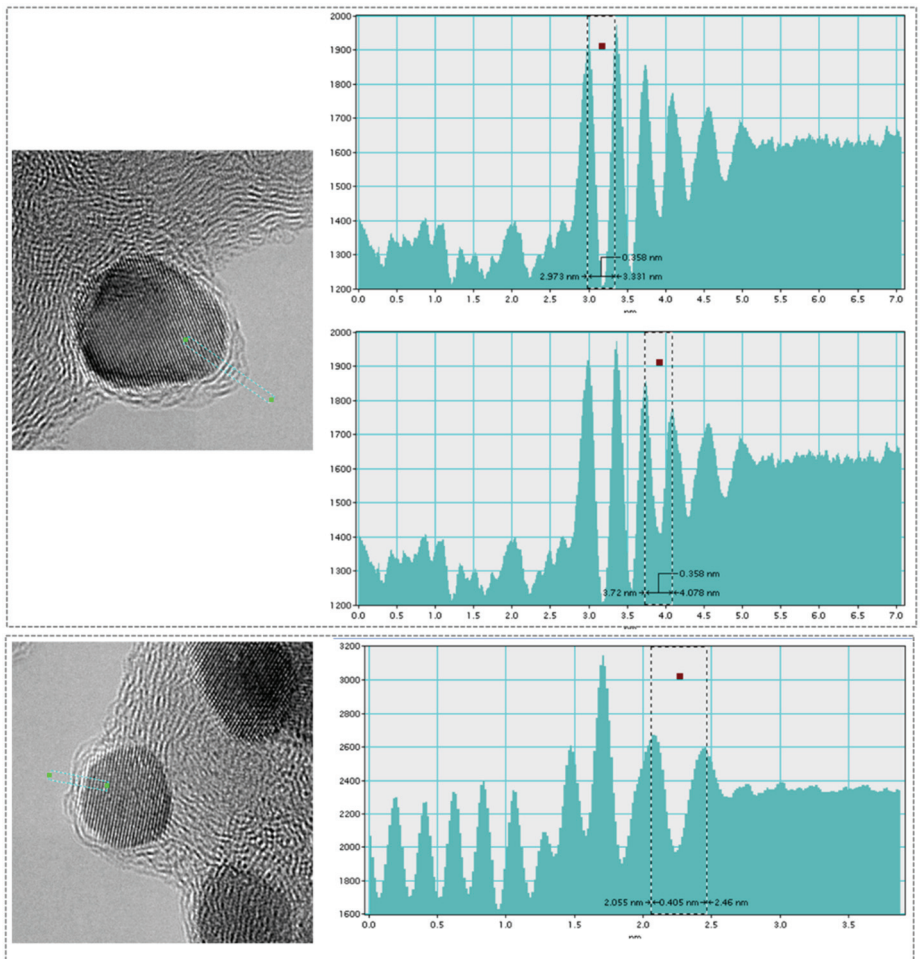

Figure 3.5.2. TEM analysis of the carbon-carbon interlayer distance. TEM images the samples with dopamine coating of 2 hr. The average thickness of each carbon layer is 0.43 ± 0.06 nm.

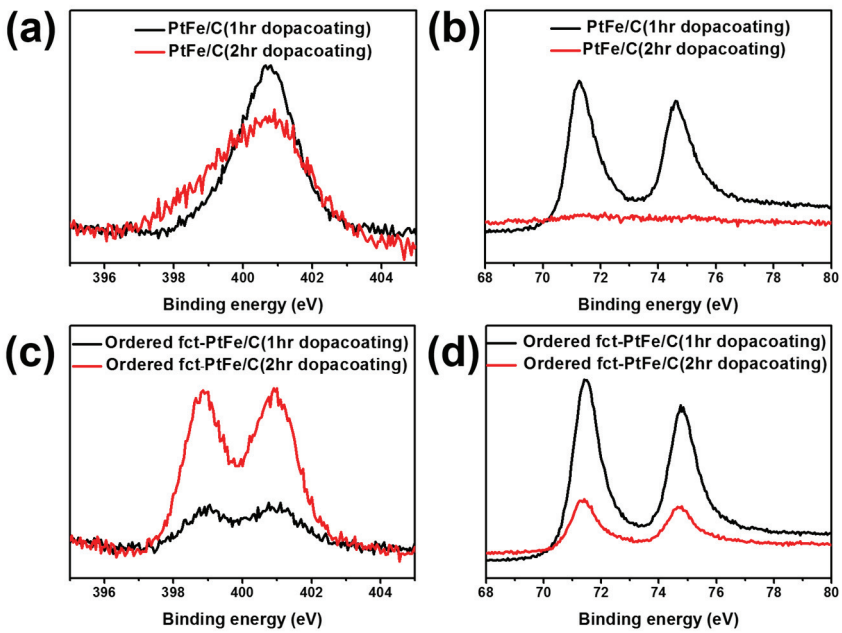

Figure 3.6. HR-PES analysis of polydopamine-coated (a-b) and N-doped carbon-coated (c-d) NPs with different coating times. PES signals from N1s are shown in panels a and c, and Pt 4f in panels b and d (hν = 630 eV, PAL 8A1 beamline).

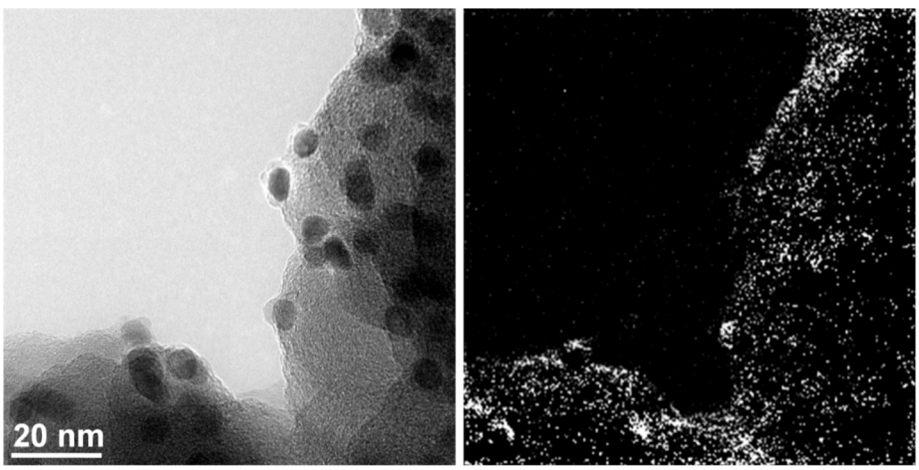

Figure 3.7. Bright field (left) and energy-filtered (right) TEM images of ordered fct-PtFe/C with coating time of 2 hr showing the distribution of nitrogen.

3.3.2 Electrochemical Tests of PtFe Nanocatalysts

The electrocatalytic properties of N-doped carbon shell-coated ordered fct-PtFe/C nanocatalyst are investigated by performing oxygen reduction reaction (ORR) using a rotating disk electrode. For comparison, disordered fcc-PtFe/C nanocatalyst is prepared by thermal annealing of PtFe NPs at 400 ºC instead of 700 ºC (**Figure 3.8**). Also, commercial Pt/C electrocatalyst is tested as a standard. According to ORR polarization curves in **Figure 3.9a**, ordered fct-PtFe/C shows the highest performance followed by disordered fcc-PtFe/C and Pt/C in terms of the half-wave potential. The mass activity of ordered fct-PtFe/C was 1.6 $A \cdot mg^{-1}$, which is 11.4 times higher than that of Pt/C (0.14 $A \cdot mg^{-1}$, **Figure 3.9b** and **Table 3.1**). The specific activity of ordered fct-PtFe/C (2.3 $mA \cdot cm^{-2}$) is also improved by 10.5 times compared to Pt/C (0.22 $mA \cdot cm^{-2}$). In order to study the relationship of these enhanced catalytic properties to the ordered fct structure of PtFe/C, various structural analyses are performed. In general, increase in electrocatalytic activity for ORR is attributed to the change in the oxygen adsorption energy by electronic structure modification[36-38] and geometric effects.[39,40] HR-PES and X-ray absorption near edge structure (XANES) spectroscopy

measurements reveal modification of d-band structure of ordered fct-PtFe NPs compared to pure Pt (**Figure 3.10**). In addition, according to HRPD (**Figure 3.1d**) and extended X-ray absorption fine structure (EXAFS) analysis (**Figure 3.11** and **Table 3.2**), ordered fct-PtFe NPs have smaller lattice constant and shorter Pt-Pt and Pt-Fe bond lengths compared to disordered fcc-PtFe NPs. Combining the electronic structure and strain analysis data, we conclude that ordered fct-PtFe NPs have lower oxygen adsorption energy compared to disordered fcc-PtFe NPs and Pt/C, leading to the enhanced electrocatalytic activity. (**Figure 3.10 and 3.11**). Moreover, the lower OH adsorption is supported by the cyclic voltammograms (CV) (**Figure 12**). The OH adsorption peak is positively shifted significantly in the case of fct-PtFe/C, which suggests low oxygen adsorption intensity. To test the possibility of any contribution of N-doped carbon shell to the catalytic activity, we prepared N-doped carbon shell-coated Pt/C (**Figure 13**) and tested it under the same condition as the data in Figure 3a. The result shows negligible effect of the shell on the activity, which confirms that the enhancement in the ORR activity is originated from ordered fct structure of PtFe NPs.

Recently, it was reported that N-doped carbon-coated metal (Fe and Co) structures showed electrocatalytic activity for ORR.[41,42] Therefore, we investigated whether the observed activity of ordered fct-PtFe/C is originated from the carbon shell or metal core by using calix[4]arene thiol derivative, which is a well-known oxygen inhibitor in ORR due to its strong binding ability to the surface of electrocatalyst with its thiol group.[43,44] In a control experiment, Pt/C modified with calix[4]arene thiol derivative is almost completely deactivated, proving the deactivation ability of this compound (**Figure 3.14**). In **Figures 3.9c** and 3.9d, ORR polarization curves before and after calix[4]arene thiol derivative modification are compared for ordered fct-PtFe/C with thin (< 1nm) and thick (3.5 nm) N-doped carbon shells, respectively. In the data from both thin and thick shell samples, the thiol modification leads to deactivation of the catalytic activity, confirming that ORR takes place at the surface of PtFe NPs. At the same time, this result confirms that the thin carbon shell is permeable for the molecules as large as calix[4]arene and, thus, will not hamper the mass transport of molecular oxygen. This high permeability is in agreement the previous studies on the carbon shell-encapsulated nanoparticles.[34] On the other hand, if the thickness

of the shell increases, it becomes much harder for the reactant to reach the surface of the NPs, as depicted in **Figure 3.9e**.

Long-term stability of electrocatalyst is a critically important issue in electrochemical applications and fuel cell commercialization.[45] We conducted an accelerated durability test (ADT) under Ar for 10,000 potential cycles between 0.6 and 1.0 V vs. RHE to test the stability of our nanocatalyst and the results are shown in **Figures 3.15a and 3.15b** (for the full data set, see **Figure 3.16 and 3.17**). The data clearly reveal that ordered fct-PtFe/C exhibits superior long-term stability with negligible activity loss compared to Pt/C and disordered fcc-PtFe/C. Ordered fct-PtFe/C also shows good stability in ADT under O_2 saturated condition (**Figure 3.15b**). According to cyclic voltammetry data, there is only little change in the current density of hydrogen underpotential deposition region (0-0.36 V) for ordered fct-PtFe/C after ADT both in Ar and O2 conditions, indicating small loss of the electrochemical surface area (**Figure 3.16**). On the other hand, disordered fcc-PtFe/C and Pt/C show significant decrease in the electrochemical surface area after ADT. For the long term test under the full cell condition, we fabricated membrane electrode assembly (MEA), which is close to the realistic fuel

cell operating condition, and performed continuous operation of 100 hr (**Figure 3.15c-3.15e**). In this test, ordered fct-PtFe/C clearly demonstrates the higher stability with the loss in the maximum power density of only 3.4%. Compared to the loss of 27% observed from commercial Pt/C catalyst, this result demonstrates extremely high durability of our ordered fct-PtFe/C.

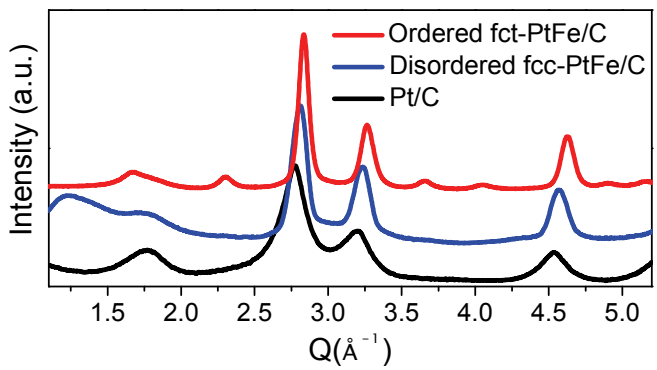

Figure 3.8. HRPD data of ordered fct-PtFe/C, disordered fcc-PtFe/C (400 ^{o}C annealed) and Pt/C.

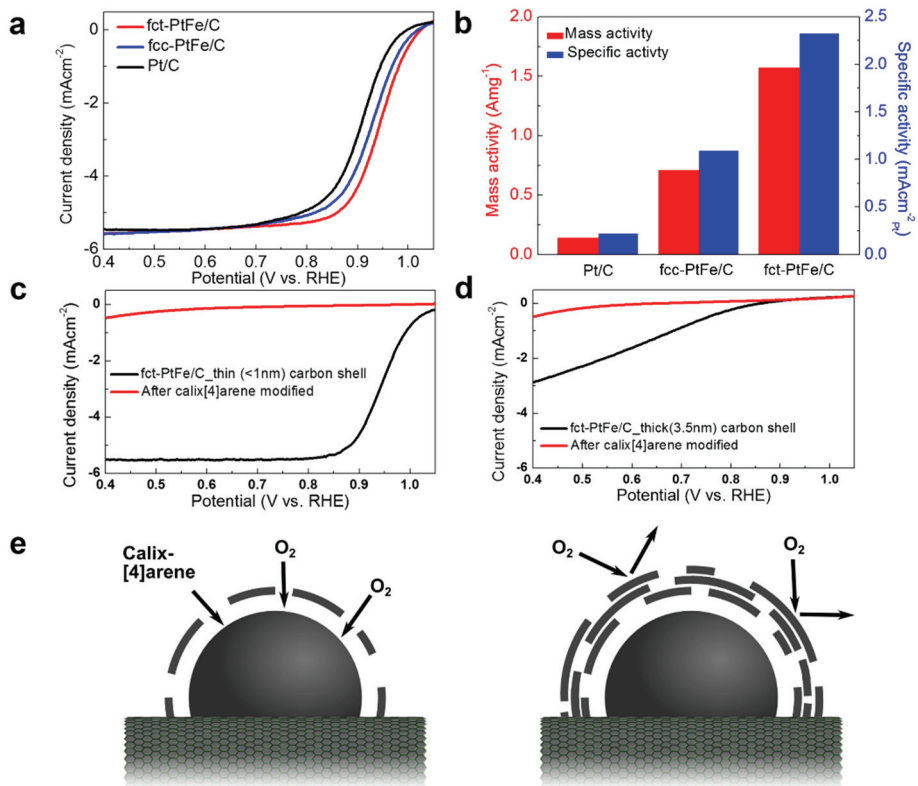

Figure 3.9. Electrochemical oxygen reduction reaction activity. (a) Oxygen reduction reaction activity of ordered fct-PtFe/C, disordered fcc-PtFe/C, and Pt/C measured using 1600 rpm rotating disc electrode. (b) Mass and specific activities of the electrodes measured at 0.9 V. (c-d) ORR activity of ordered fct-PtFe nanocatalysts modified with calix[4]arene thiol derivative with thin (c, < 1nm) and thick (d, 3.5 nm) carbon shells. (e) Schematic diagrams of active sites with respect to the carbon shell thickness

	mass activity (A/mgPt) @0.9V RT	specific activity (mA/cm2) @ 0.9V RT	ref
DOE 2020 target	0.44		
Pd-Pt nanodendritres	0.24	0.42	[6]
Pt3Ni octahedra	0.11	2.8	[7]
Acid treated/annealed PtNi/C	~0.34 (0.95 V 60°C)	0.85 (0.95 V 60°C)	[8]
Au/FePt3/C	~0.55	1.5	[9]
PtNi	0.68	3.0	[10]
Icosahedraon Pt3Ni	0.94	2.78	[11]
Pt3Ni nanoframe	5.7 (0.9 V) 0.95(0.95 V)	~1.5(0.95 V)	[12]
Nanoporous-Pt6Ni1	0.65	1.23	[13]
Pt2.5Ni/C octahedra	3.3	5.1(0.93 V)	[14]
Ordered fct-PtFe/C	1.6	2.3	Current study

Table 3.1. ORR activity data from the previous literatures. All the potentials are referred to RHE.

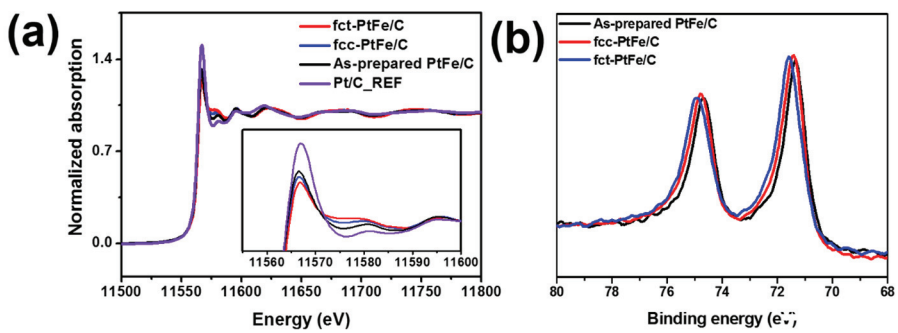

Figure 3.10. (a) Pt L_3 XANES (PAL 8C) and (b) HR-PES analysis (hν = 630 eV, PAL 8A1) of ordered fct-PtFe/C, disordered fcc-PtFe/C, as-prepared PtFe/C, and Pt/C. In panel a, the whiteline intensity of Pt L3-edge signal from ordered fct-PtFe/C is the smallest among the samples, which suggests the decrease in Pt vacancy through electronic perturbation with Fe. Also, the high binding energy of Pt 4f PES signal from ordered fct-PtFe/C in panel b implies the modification of d-band structure.

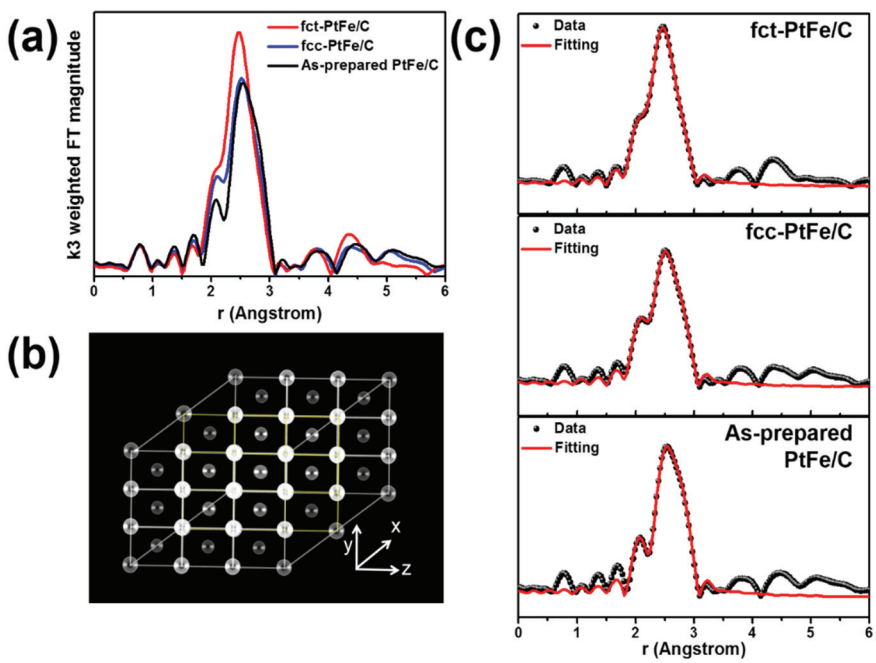

Figure 3.11. EXAFS data of various PtFe nanocatalysts. (a) k^3 weight FT magnitude spectra of Pt L_3-edge. (b) Model structure of ordered fct-PtFe. (c) Fitting results of the EXAFS data.

	Pt-Pt distance (Å)	Pt-Pt coordination number (N)	Pt-Fe distance (Å)	Pt-Fe coordination number(N)	Reduced Chi square value	R-factor
As-prepared PtFe/C	2.7480(8)	6.50(6)	2.6822(9)	0.93(1)	33.1	0.0081
Disordered fcc-PtFe/C	2.7371(9)	5.50(7)	2.6722(1)	2.44(9)	69.0	0.0043
Ordered fct-PtFe/C	2.7214(4)	4.26(5)	2.6730(2)	3.86(6)	13.9	0.0012

Table 3.2. EXAFS fitting results

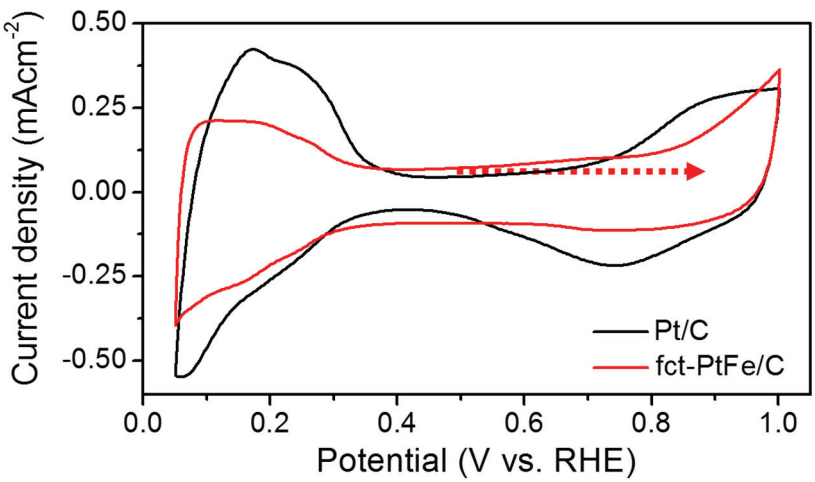

Figure 3.12. Cyclic voltammograms of Pt/C and fct-PtF/C

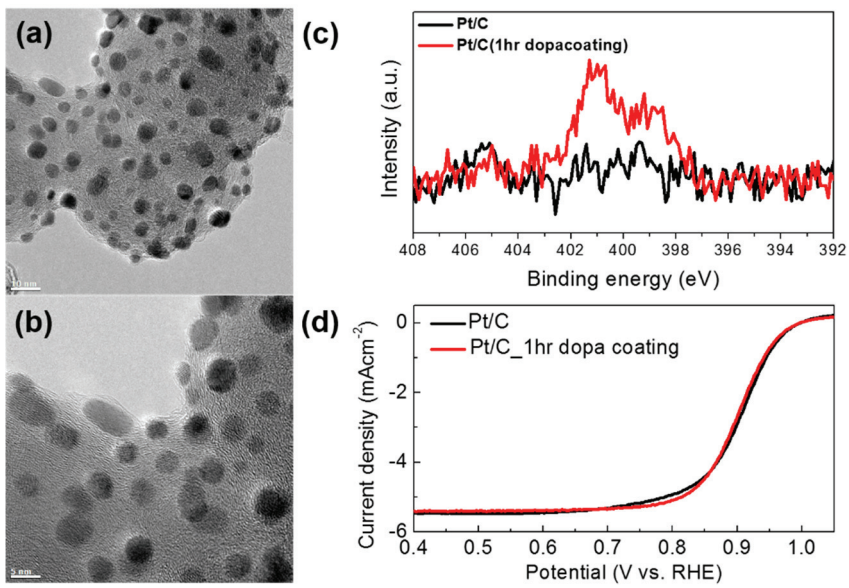

Figure 3.13. Comparison of dopamine coating effects on bare Pt/C (a,b) TEM image of 1 hr dopamine coating Pt/C with 700 ºC heat treatment, (c) N 1s XPS spectra (d) ORR activity

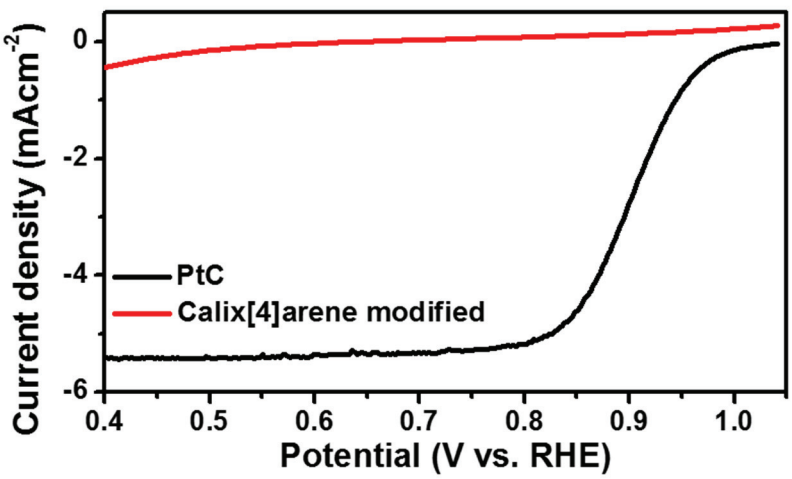

Figure 3.14. ORR activity comparison of Pt/C before and after calix[4]arene modified.

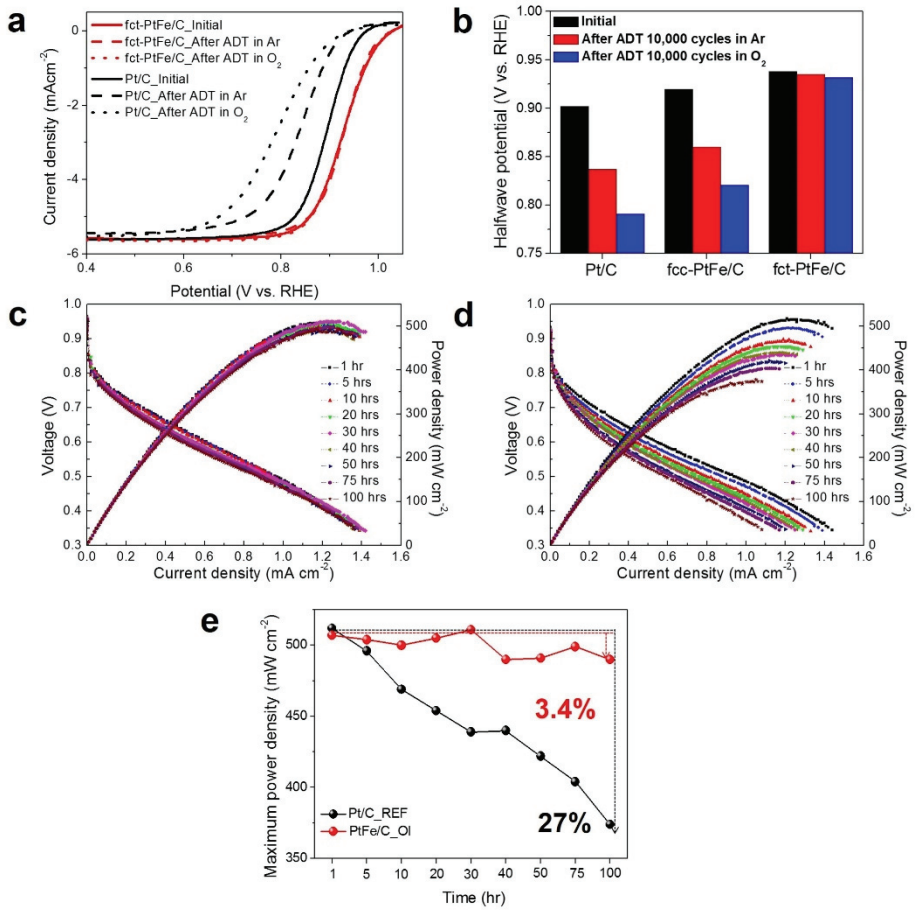

Figure 3.15. Long-term stability test before and after ADT. (a-b) ORR polarization curves (a) and changes in half wave potentials (b) of Pt/C, fcc-PtFe/C, and fct-PtFe/C before and after ADT of 10,000 cycles. (c-e) Results from 100 hr MEA test for fct-PtFe/C (c) and Pt/C (d) and their maximum power density plot as functions of operating time (e).

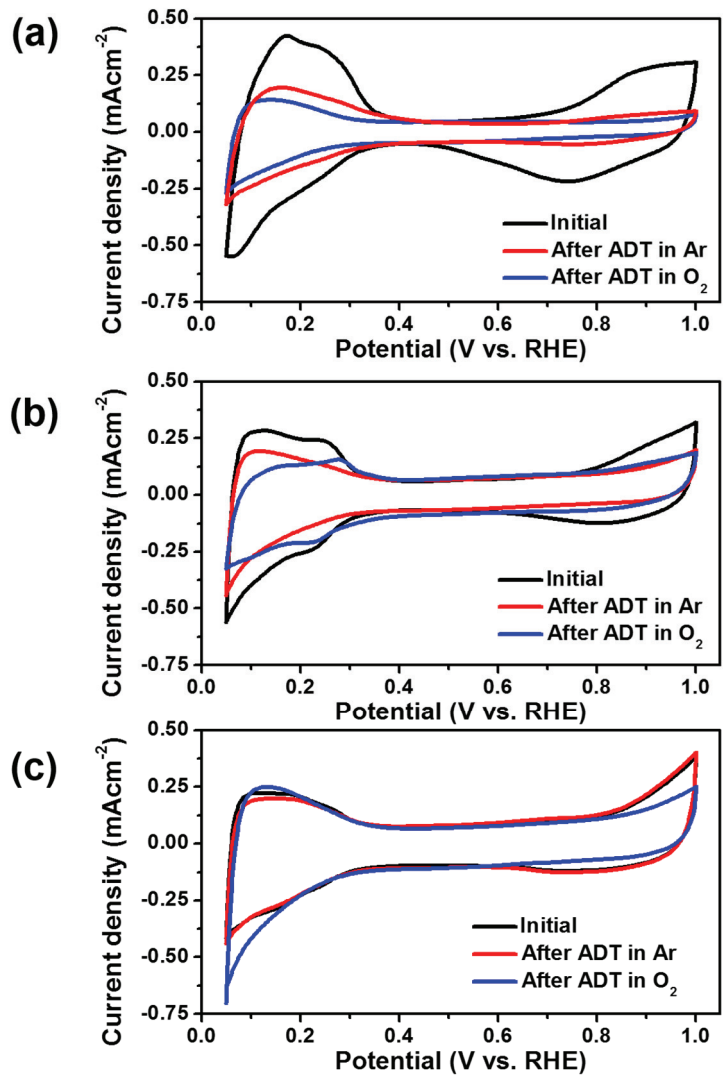

Figure 3.16. CVs of initial and after ADT 10,000 cycles for (a) Pt/C, (b) disordered fcc-PtFe/C and (c) ordered fct-PtFe/C.

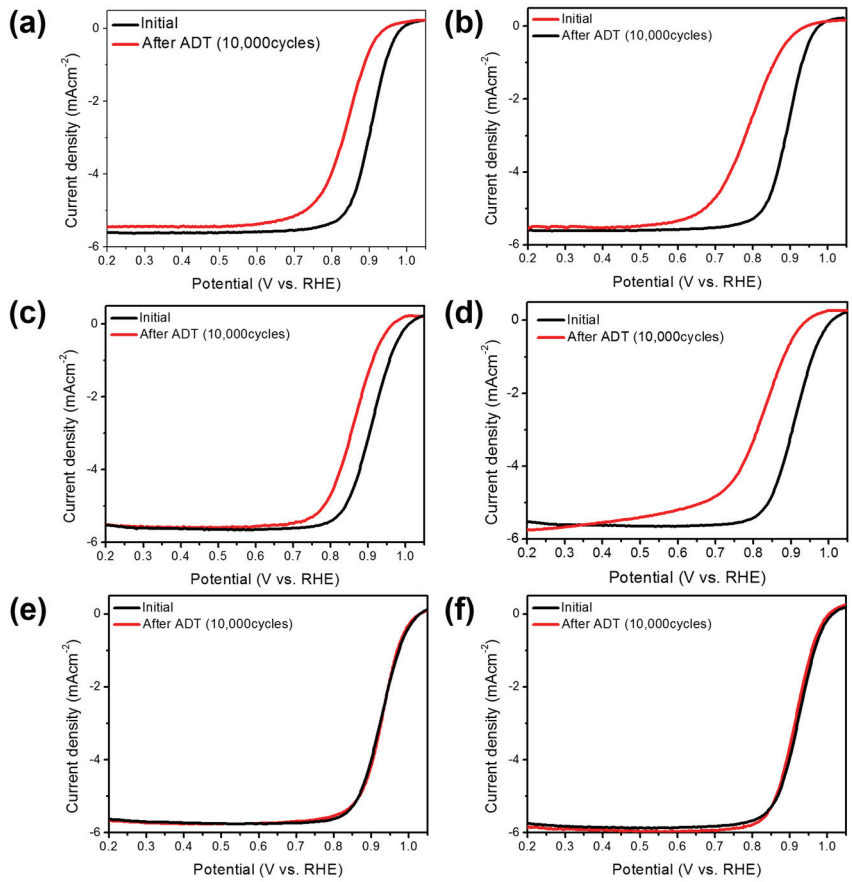

Figure 3.17. Long-term durability test of Pt/C (a and b), disordered fcc-PtFe/C (c and d), ordered fct-PtFe/C (e and f). The atmosphere was Ar for the data in panels (a,c and e) and O_2 in panel (d, e and f).

3.3.3 Structural Analysis of Ordered fct-PtFe Nanocatalyst

In order to investigate the role of Pt-Fe alloy structures for the durability of nanocatalyst, we conducted *in situ* XANES measurements on Pt L_3-edge of ordered fct-PtFe/C, disordered fcc-PtFe/C, and Pt/C in Ar-saturated 0.1 M $HClO_4$ solution with the potential range from 0.6 to 1.2 V vs. RHE. In these measurements, the extent of Pt oxidation is estimated by the whiteline intensity of XANES spectrum which reflects the amount of Pt d-band vacancy as a function of potential (**Figure 3.18a**, see **Figure 3.19** for XANES spectra).[46,47] As mentioned above, oxidation of Pt atoms is one of the major deactivation mechanisms of the fuel cell electrocatalyst. By alloying with Fe, Pt atoms become more oxidation-resistive with the higher oxidation potentials than pure Pt.[48] According to the *in situ* XANES data, ordered fct-PtFe/C is more oxidation-resistant than the other two samples. Especially, comparing the PtFe/C samples measured after ADT, the extent of Pt oxidation of ordered fct-PtFe/C is less than half of that of disordered fcc-PtFe/C at 1.2 V. Considering that Pt atoms of Pt-Fe alloy becomes easier to be oxidized as more Fe atoms are dissolved from the alloy during ADT, we conclude that Fe atoms in ordered fct-PtFe structure are more stable and less dissolved than those

in disordered fcc-PtFe. Experimental evidence of dissolution-resistive Fe atoms in ordered fct-PtFe is found from energy dispersive spectroscopy (EDS) analysis of the samples after 10,000 ADT cycles (**Figure 18b**). The elemental mapping images of Pt and Fe match well to STEM image of ordered fct-PtFe, indicating stable PtFe intermetallic structure of the NPs. In contrast, for disordered fcc-PtFe, the mapping image of Fe has no resemblance to either Pt mapping or STEM images. The atomic ratios of Pt and Fe from EDS data show that the amount of Fe in disordered fcc-PtFe is significantly decreased from Pt:Fe = 51:49 to 90:10 after ADT due to extensive dissolution of Fe, while the change in the atomic ratio of ordered fct-PtFe is minimal from 51:49 to 58:42 (see **Table 3.3** for atomic ratios and **Figure 3.20** for EDS line scan data of NPs. In addition to the contribution of ordered fct structure to the high durability, previous reports suggest that the encapsulation by carbon shell not only provides physical barrier to prohibit the particle agglomeration but also stabilize the surface of the nanoparticles, both of which help to maintain the small size and high activity of the nanoparticles during the electrochemical reaction.[28] We also conjectured that the physical and chemical protection of N-doped carbon shell is responsible for the high

stability in the long-term operation of catalyst.

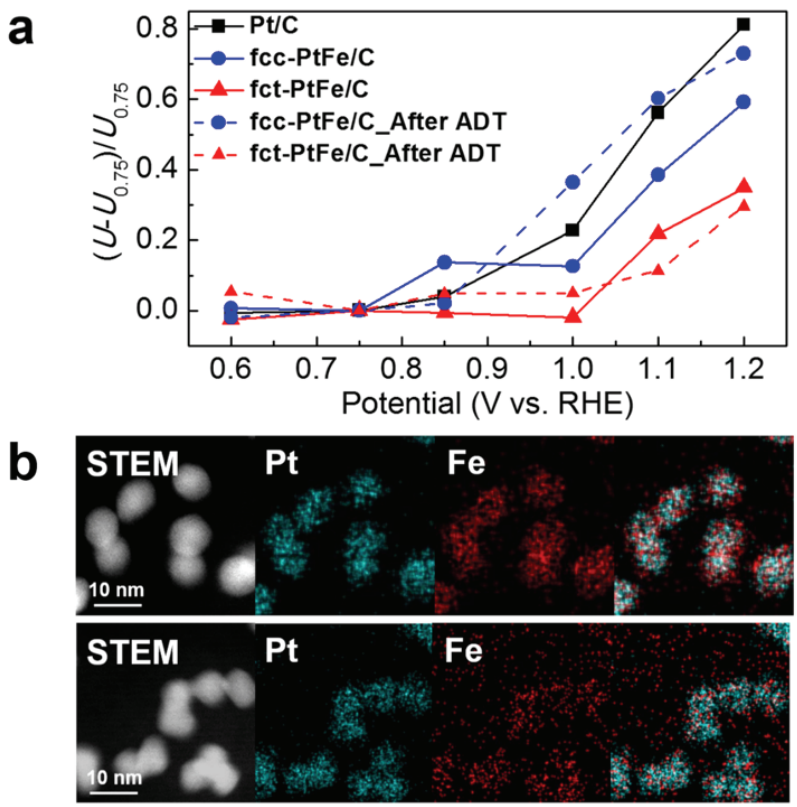

Figure 3.18. Long-term stability analysis through *in situ* XANES, computational analysis and TEM. (a) Change in the whiteline intensity of Pt L_3-edge as functions of potential measured by *in situ* XANES analysis. U and $U_{0.75}$ indicate the integrated whiteline intensity and the value of U at 0.75 V, respectively (b) HAADF-STEM and EDS elemental mapping analysis of ordered fct-PtFe/C (up) and disordered fcc-PtFe/C (down) after ADT 10,000 cycles.

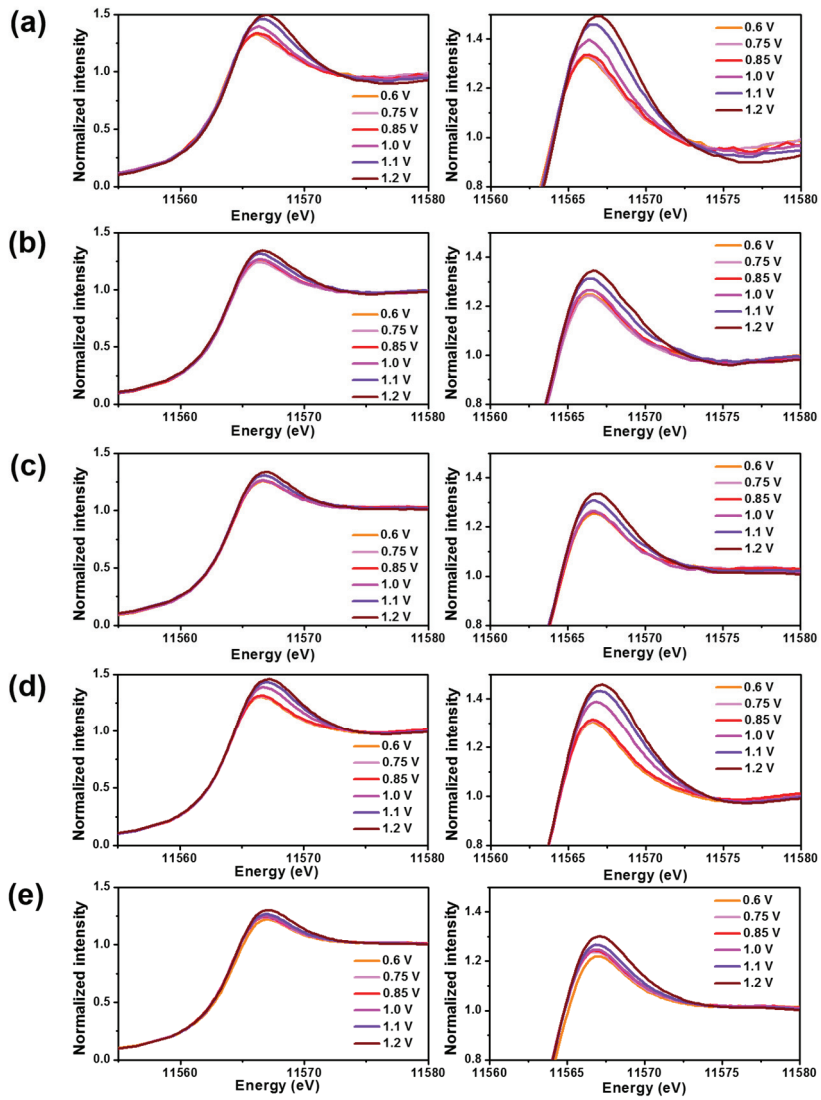

Figure 3.19. *In situ* XANES analysis of Pt/C (a), disordered fcc-PtFe/C (b) and ordered fct-PtFe/C (c) before ADT, disordered fcc-PtFe/C (d), and ordered fct-PtFe/C (e) after ADT 10,000 cycles.

Sample	Atomic ratio of Pt:Fe (standard deviation)
Ordered fct-PtFe/C	51.4 : 48.6 (0.55)
Disordered fcc-PtFe/C	50.9 : 49.1 (0.92)
Ordered fct-PtFe/C after ADT	58.2 : 41.8 (0.85)
Disordered fcc-PtFe/C after ADT	90.1 : 9.9 (0.67)

*These values were acquired TEM EDS analysis and averaged at 5 different regions.

Table 3.3. Atomic ratio (Pt:Fe) of nanoparticles before and after ADT

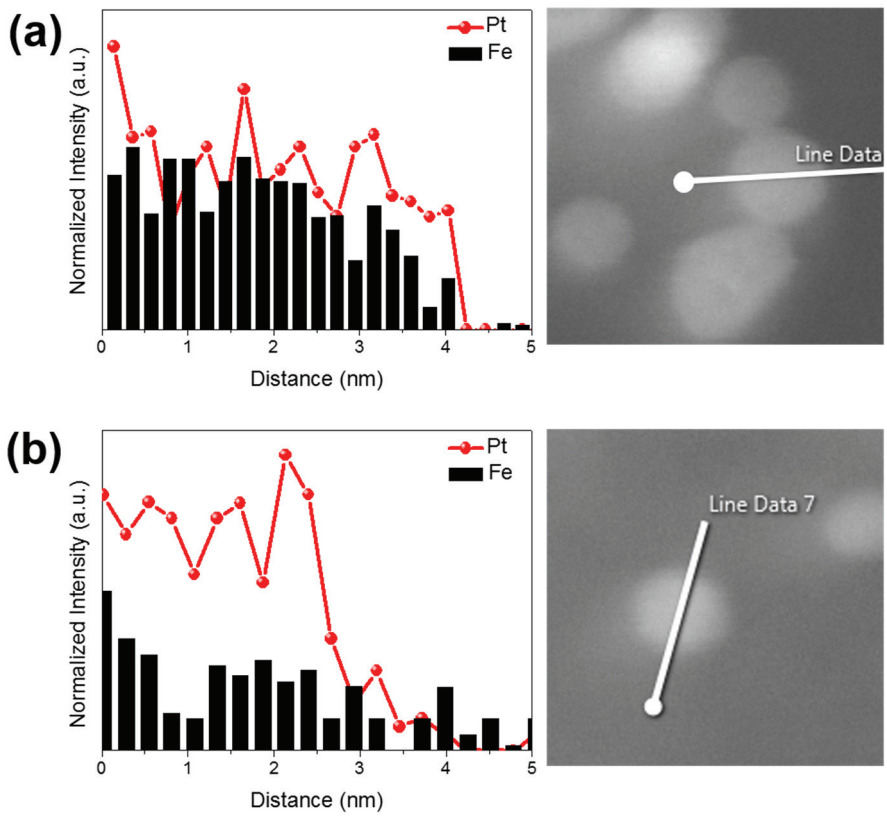

Figure 3.20. EDS line scan analysis data of ordered fct-PtFe/C (a) and disordered fcc-PtFe/C (b) after ADT 10,000 cycles.

3.4 Conclusion

In conclusion, we present a new and very effective approach to prepare highly active and stable fuel cell electrocatalyst by encapsulating carbon-supported PtFe NPs with the dual purpose N-doped carbon shell. This shell is *in situ* formed during thermal annealing of fcc-PtFe NPs to transform them into ordered fct structure. The N-doped carbon shell not only prevents the coalescence of the NPs during thermal annealing process to keep their sizes as small as ~ 6.5 nm, but also protects them in harsh fuel cell operating conditions. We found that, when the thickness of the carbon shell less than 1 nm, the shell is highly permeable so that the catalytic activity is not affected but the NPs are well protected. Our ordered fct-PtFe/C nanocatalyst coated with N-doped carbon shell shows the higher performance compared to disordered fcc-PtFe/C and commercial Pt/C. Furthermore, ADT and MEA tests show that ordered fct-PtFe/C exhibits much higher long-term stability without significant activity loss. *In situ* XANES and EDS studies reveal that ordered fct-PtFe structure and the presence of N-doped carbon shell are critical for the excellent performance of our nanocatalyst. We believe that this

approach can open a new possibility for the development of high performance and cost-effective fuel cell catalysts in the near future.

3.5 References

[1]. Jung, N.; Chung, D. Y.; Ryu, J.; Yoo, S. J.; Sung, Y. E. Nano Today 2014, 9, 433-456.

[2]. Lim, B.; Jiang, M.; Camargo, P. H. C.; Cho, E. C.; Tao, J.; Lu, X.; Zhu, Y.; Xia, Y. Science 2009, 324, 1302-1305.

[3]. Chen, C.; Kang, Y.; Huo, Z.; Zhu, Z.; Huang, W.; Xin, H. L.; Snyder, J. D.; Li, D.; Herron, J. A.; Mavrikakis, M.; Chi, M.; More, K. L.; Li, Y.; Markovic, N. M.; Somorjai, G. A.; Yang, P.; Stamenkovic, V. R. Science 2014, 343, 1339-1343.

[4]. Zhang, S.; Hao, Y.; Su, D.; Doan-Nguyen, V. V. T.; Wu, Y.; Li, J.; Sun, S.; Murray, C. B. J. Am. Chem. Soc. 2014, 136, 15921.-15924.

[5]. Guo, S.; Zhang, S.; Sun, S. Angew. Chem. Int. Ed. 2013, 52, 8526-8544.

[6]. Stephens, I. E. L.; Bondarenko, A. S.; Grønbjerg, U.; Rossmeisl, J.; Chorkendorff, I. Energy Environ. Sci. 2012, 5, 6744-6762.

[7]. Huang, X.; Zhao, Z.; Cao, L.; Chen, Y.; Zhu, E.; Lin, Z.; Li, M.;

Yan, A.; Zettl, A.; Wang, Y. M.; Duan, X.; Mueller, T.; Huang, T. Science 2015, 348, 1230-1234.

[8]. Zhang, L.; Roling, L. T.; Wang, X.; Vara, M.; Chi, M.; Liu, J.; Choi, S. –I.; Park, J.; Herron, J. A.; Xie, Z.; Mavrikakis, M.; Xia, Y. Science 2015, 349, 412-416.

[9]. Wu, J.; Yang, H. Acc. Chem. Res. 2013, 46, 1848-1857.

[10]. Porter, N. S.; Wu, H.; Quan, Z.; Fang, J. *Acc. Chem. Res.* **2013**, *46*, 1867-1877.

[11]. You, H.; Yang S.; Ding, B.; Yang, H. *Chem. Soc. Rev.* **2013**, *42*, 2880-2904.

[12]. Wang, D.; Li, Y. *Adv. Mater.* **2011**, *23*, 1044-1060.

[13]. Bing, Y.; Liu, H.; Zhang, L.; Ghosh, D.; Zhang, J.J. *Chem. Soc. Rev.* **2010**, *39*, 2184-2202.

[14]. Zhang, L.; Iyyamperumal, R.; Yancey, D. F.; Crooks, R. M.; Henkelman, G. *ACS Nano* **2013**, *7*, 9168-9172.

[15]. Ferreira, P. J.; La O, G. J.; Shao-Horn, Y.; Morgan, D.; Makharia, R.; Kocha, S.; Gasteiger, H. A. *J. Electrochem. Soc.* **2005**, *152*, A2256-A2271.

[16]. Tang, L.; Han, B.; Persson, K.; Friesen, C.; He, T.; Sieradzki, K.; Ceder, G. *J. Am. Chem. Soc.* **2010**, *132*, 596-600.

[17]. Kim, J.; Lee, Y.; Sun, S. *J. Am. Chem. Soc.* **2010**, *132*, 4996-4997.

[18]. Wang, D.; Xin, H. L.; Hovden, R.; Wang, H.; Yu, Y.; Muller, D. A.; Disalvo, F. J.; Abruña, H. D. *Nat. Mater.* **2013**, *12*, 81-87.

[19]. Kang, Y.; Pyo, J. B.; Ye, X.; Gordon, T. R.; Murray, C. B. *ACS Nano* **2012**, *6*, 5642-5647.

[20]. Li, Q.; Wu, L.; Wu, G.; Su, D.; Lv, H.; Zhang, S.; Zhu, W.; Casimir, A.; Zhu, H.; Mendoza-Garcia, A.; Sun, S. *Nano Lett.* **2015**, *15*, 2468-2473.

[21]. Ghosh, T.; Vukmirovic, M. B.; DiSalvo, F. J.; Adzic, R. R. *J. Am. Chem. Soc.* **2010**, *132,* 906-907.

[22]. Wang, D.; Yu, Y.; Xin, H. L.; Hovden, R.; Ercius, P.; Mundy, J. A.; Chen, H.; Richard, J. H.; Muller, D. A.; Disalvo, F. J.; Abruña, H. D. *Nano Lett.* **2012**, *12*, 5230-5238.

[23]. Wang, G.; Huang, B.; Xiao, L.; Ren, Z.; Chen, H.; Wang, D.; Abruña, H. D.; Lu, J.; Zhuang, L. *J. Am. Chem. Soc.* **2014**, *136*, 9643-9649.

[24]. Rong, C. B.; Li, D.; Nandwana, V.; Poudyal, N.; Ding, Y.; Wang, Z. L.; Zeng, H.; Liu, J. P. *Adv. Mater.* **2006**, *18*, 2984-2988.

[25]. Lee, D. C.; Mikulec, F. V.; Pelaez, J. M.; Koo, B.; Korgel, B. *J. Phys. Chem. B* 2006, *110,* 11160-11166.

[26]. Chen, H.; Wang, D.; Yu, Y.; Newton, K. A.; Muller, D. A.; Abruña, H.; Disalvo, F. J. *J. Am. Chem. Soc*. **2012**, *134*, 18453-18459.

[27]. Holby, E. F.; Sheng, W.; Shao-Horn, Y.; Morgan, D. *Energy Environ. Sci.* **2009**, *2*, 865-871.

[28]. Guo, L.; Jiang, W. J.; Zhang, Y.; Hu, J. S.; Wei, Z. D.; Wan, L. J. *ACS Catal.* **2015**, *5*, 2903-2909.

[29]. Cheng, N.; Banis, M. N.; Liu, J.; Riese, A.; Li, X.; Li, R.; Ye, S.; Knights, S.; Sun, X. *Adv. Mater.* **2015**, *27*, 277-281.

[30]. Baldizzone, C.; Mezzavilla, S.; Carvalho, H. W. P.; Meier, J. C.; Schuppert, A. K.; Heggen, M.; Galeano, C.; Grunwaldt, J. D.; Schüth, F.; Mayrhofer, K. J. J. *Angew. Chem. Int. Ed.* **2014**, *53*, 14250-14254.

[31]. Galeano, C.; Meier, J. C.; Peinecke, V.; Bongard, H.;

Katsounaros, I.; Topalov, A. A.; Lu, A.; Mayrhofer, K. J. J.; Schüth, F. *J. Am. Chem. Soc.* **2012**, *134*, 20457-20465.

[32]. Pylypenko, S.; Borisevich, A.; More, K. L.; Corpuz, A. R.; Holme, T.; Dameron, A. A.; Olson, T. S.; Dinh, H. N.; Gennett, T.; O'Hayre, R. *Energy Environ. Sci.* **2013**, *6*, 2957-2964.

[33]. Zhang, S.; Zhang, X.; Jiang, G.; Zhu, H.; Guo, S.; Su, D.; Lu, G.; Sun, S. *J. Am. Chem. Soc.* **2014**, *136*, 7734-7739.

[34]. Liu, R.; Mahurin, S. M.; Li, C.; Unocic, R. R.; Idrobo, J. C.; Gao, H.; Pennycook, S. J.; Dai, S. Angew. Chem. Int. Ed. 2011, 50, 6799-6802.

[35]. Lee, H.; Dellatore, S. M.; Miller, W. M.; Messersmith, P. B. *Science* **2007**, *318*, 426-430.

[36]. Stamenkovic, V. R.; Fowler, B.; Mun, B. S.; Wang, G.; Ross, P. N.; Lucas, C. A.; Markovic, N. M. *Science* **2007**, *315*, 493-497.

[37]. Hwang, S. J.; Kim, S. K.; Lee, J. G.; Lee, S. C.; Jang, J. H.; Kim, P.; Lim, T. H.; Sung, Y.E.; Yoo, S. J. *J. Am. Chem. Soc.* **2012**, *134*, 19508-19511.

[38]. Kim, Y. S.; Jeon, S. H.; Bostwick, A.; Rotenberg, E.; Ross, P. N.; Stamenkovic, V. R.; Markovic, N. M.; Noh, T. W.; Han, S.;

Mun, B. S. *Adv. Energy Mater.* **2013**, *3*, 1257-1261.

[39]. Strasser, P.; Koh, S.; Anniyev, T.; Greeley, J.; More, K.; Yu, C.; Liu, Z.; Kaya, S.; Nordlund, D.; Ogasawara, H.; Toney, M. F.; Nilsson, A. *Nat. Chem.* **2010**, *2*, 454-460.

[40]. Min, M. K.; Cho, J.; Cho, K.; Kim, H. *Electrochim. Acta* **2000**, *45*, 4211-4217.

[41]. Wu, G.; More, K. L.; Johnston, C. M.; Zelenay, P. *Science* **2011**, *332*, 443-447.

[42]. Chung, H. T.; Won, J. H.; Zelenay, P. *Nat. Commun.* **2013**, *4*, 1922-1925.

[43]. Genorio, B.; Strmcnik, D.; Subbaraman, R.; Tripkovic, D.; Karapetrov, G.; Stamenkovic, V. R.; Pejovnik, S.; Marković, N. M. *Nat. Mater.* **2010**, *9*, 998-1003.

[44]. Genorio, B.; Subbaraman, R.; Strmcnik, D.; Tripkovic, D.; Stamenkovic, V. R.; Markovic, N. M. *Angew. Chem. Int. Ed.* **2011**, *50*, 5468-5472.

[45]. Debe, M. K. *Nature* **2012**, *486*, 43-51.

[46]. Zhang, J.; Sasaki, K.; Sutter, E.; Adzic, R. R. *Science* **2007**, *315*, 220-222.

[47]. Friebel, D.; Miller, D. J.; Nordlund, D.; Ogasawara, H.; Nilsson, A. *Angew. Chem. Int. Ed.* **2011**, *50*, 10190-10192.

[48]. Stamenkovic, V. R.; Mun, B. S.; Arenz, M.; Mayrhofer, K. J. J.; Lucas, C. A.; Wang, G.; Ross, P. N.; Markovic, N. M. *Nat. Mater.* **2007**, *6*, 241-247.

[49]. Wei, G. F.; Liu, Z. P. *Energy Environ. Sci.* **2011**, *4*, 1268-1272.

[50]. Li, D.; Wang, C.; Tripkovic, D.; Sun, S.; Markovic, N. M.; Stamenkovic, V. R. *ACS Catal.* **2012**, *2*, 1358-1362.

Bibliography

1. Journal Publication

1) Dong Young Chung, **Samuel Woojoo Jun** (*co-first author*), Gabin Yoon, Soon Gu Kwon, Dong Yun Shin, Pilseon Seo, Ji Mun Yoo, Heejong Shin, Young-Hoon Chung, Hyunjoong Kim, Bongjin Simon Mun, Kug-Seung Lee,Δ Nam-Suk Lee, Sung Jong Yoo, Dong-Hee Lim, Kisuk Kang, Yung-Eun Sung and Taeghwan Hyeon

"Highly Durable and Active PtFe Nanocatalyst for Electrochemical Oxygen Reduction Reaction."

Journal of the American Chemical Society, **2015,** 137, 15478-15485

2) **Samuel Woojoo Jun** (*co-first author*), Mohammadreza Shokouhimehr, Dong Jun Lee, Youngjin Jang, Jinkyung Park and Taeghwan Hyeon,

"One-pot synthesis of magnetically recyclable mesoporous silica supported acid-base catalysts for tandem reactions."

Chemical Communications, **2013**, 49**,** 7821–7823

3) Kwang-Hyun Choi, Youngjin Jang, Dong Young Chung, Pilseon Seo, **Samuel Woojoo Jun**, Ji Eun Lee, Myoung Hwan Oh, Mohammadreza Shokouhimehr, Namgee Jung, Sung Jong Yoo, Yung-Eun Sung and Taeghwan Hyeon
"A simple synthesis of urchin-like Pt–Ni bimetallic nanostructures as enhanced electrocatalysts for the oxygen reduction reaction."
Chemical Communications, **2016**, 52**,** 597–600

4) Donghee Son, JonghaLee, Shutao Qiao, Roozbeh Ghaffari, JaeminKim, Ji Eun Lee, Changyeong Song, Seok Joo Kim, DongJun Lee, **Samuel Woojoo Jun**, Shixuan Yang ,Minjoon Park, Jiho Shin, Kyungsik Do, Mincheol Lee, Kwanghun Kang, Cheol Seong Hwang, Nanshu Lu,Taeghwan Hyeon and Dae-Hyeong Kim
"Multifunctional wearable devices for diagnosis and therapy of movement disorders."

Nature Nanotechnology, **2014**, 9**,** 397–404

5) Mohammadreza Shokouhimehra, Taeho Kim, **Samuel Woojoo Jun**, Kwangsoo Shin, Youngjin Janga, Byung Hyo Kim, Jaeyun Kimc, Taeghwan Hyeon
"Magnetically separable carbon nanocomposite catalysts for efficient nitroarene reduction and Suzuki reactions."
Applied Catalysis A: General, **2014**, 476, 133–139

6) Mohammadreza Shokouhimehr, Keun-Young Shin, James S. Lee, Michael J. Hackett, **Samuel Woojoo Jun**, Myoung Hwan Oh, Jyongsik Jang and Taeghwan Hyeon
"Magnetically recyclable core–shell nanocatalysts for efficient heterogeneous oxidation of alcohols."
Journal of Material Chemistry A, **2014**, 2, 7593-7599

7) Radhu Subha, Venkatram Nalla, Jung Ho Yu, **Samuel Woojoo Jun**, Kwangsoo Shin, Taeghwan Hyeon, C. Vijayan and Wei Ji

"Efficient Photoluminescence of Mn 2+ -Doped ZnS Quantum Dots Excited by Two-Photon Absorption in Near-Infrared Window II."

Journal of Physical Chemistry C, **2013**, 117, 20905–20911

8) Byung Hyo Kim, Kwangsoo Shin, Soon Gu Kwon, Youngjin Jang, Hyun-Seok Lee, Hyunjae Lee, **Samuel Woojoo Jun**, Jisoo Lee, Sang Yun Han, Yong-Hyeon Yim, Dae-Hyeong Kim and Taeghwan Hyeon

"Sizing by weighing: characterizing sizes of ultrasmall-sized iron oxide nanocrystals using MALDI-TOF mass spectrometry."

Journal of American Chemical Society, **2013**, 135, 2407–10.

9) Jung Ho Yu, Seung-Hae Kwon, Zdenˇek Petrášek, Ok Kyu Park, **Samuel Woojoo Jun**, Kwangsoo Shin, Moonkee Choi, Yong Il Park, Kyeongsoon Park, Hyon Bin Na, Nohyun Lee, DongWon Lee, Jeong Hyun Kim, Petra Schwille and Taeghwan Hyeon

"High-resolution three-photon biomedical imaging using doped ZnS nanocrystals." *Nature Materials,* **2013**, 12, 359–366

10) Jinkyung Park, Soon Gu Kwon, **Samuel Woojoo Jun**, Byung Hyo Kim, and Taeghwan Hyeon
"Large-scale synthesis of ultra-small-sized silver nanoparticles."
ChemPhysChem, **2012**, 13, 2540–2543

11) Myoung Hwan Oh, Nohyun Lee, Hyoungsu Kim, Seung Pyo Park, Yuanzhe Piao, Jisoo Lee, **Samuel Woojoo Jun**, Woo Kyung Moon, Seung Hong Choi and Taeghwan Hyeon
"Large-scale synthesis of bioinert tantalum oxide nanoparticles for X-ray computed tomography imaging and bimodal image-guided sentinel lymph node mapping."
Journal of American Chemical Society, **2011**, 133, 5508–5515

12) Youngjin Jang, Seyoung Kim, **Samuel Woojoo Jun**, Byung Hyo Kim, Sunhwan Hwang, In Kyu Song, B. Moon Kim and

Taeghwan Hyeon

"Simple one-pot synthesis of Rh-Fe_3O_4 heterodimer nanocrystals and their applications to a magnetically recyclable catalyst for efficient and selective reduction of nitroarenes and alkenes."

Chemical Communications, **2011**, 47, 3601–3603

13) Youngjin Jang, Jooyoung Chung, Seyoung Kim, **Samuel Woojoo Jun**, Byung Hyo Kim, Dong Won Lee, B. Moon Kim and Taeghwan Hyeon

"Simple synthesis of Pd-Fe_3O_4 heterodimer nanocrystals and their application as a magnetically recyclable catalyst for Suzuki cross-coupling reactions."

Physical Chemistry Chemical Physics, **2011**, 13, 2512–2516

2. International Conference Presentations

1) **Samuel Woojoo Jun**, and Taeghwan Hyeon

"One-pot synthesis of magnetically recyclable mesoporous silica nanocatalyst with acid-base site-isolated functional groups for tandem reaction"

244th American Chemical Society National Meeting & Exposition, Philadelphia, Pennsylvania, U.S.A., August 19-23, 2012

2) **Samuel Woojoo Jun**, and Taeghwan Hyeon

"One-pot synthesis of magnetically recyclable mesoporous silica nanocatalyst with acid-base site-isolated functional groups for tandem reaction"

45th IUPAC World Chemistry Congress (IUPAC-2015), BEXCO, Busan, Republic of Korea, August 9-14, 2015

초 록

내구성이 뛰어난 촉매의 개발에 대한 연구는 나노촉매의 실용화 및 산업화를 위해 매우 중요하다. 본 학위 논문에서는 활성 부위 보호를 통한 내구성이 뛰어난 나노촉매의 합성과 분석에 대하여 기술한다. 유기반응 촉매에 대한 연구에서는 산 촉매와 염기 촉매를 나노재료의 표면에 고정시킴으로써 각각의 활성도를 유지 시킬 수 있었고, 전기화학 촉매에 대한 연구에서는 질소가 도핑 된 탄소막을 나노입자의 표면에 입힘으로써 합성단계에서의 열처리 과정, 또는 운행 실험 중 나노입자가 뭉치거나 떨어져 나오는 현상을 방지했다. 위에서 언급한 두 가지 접근법으로 만들어진 나노촉매들은 연속된 재사용이나 장기성능실험에서 매우 우수한 성능을 보였다.

첫번째는 유기반응촉매에 대한 연구로, 서로 상호작용하는 산 촉매와 염기 촉매를 동일한 담체에 담지하여 자성분리가 가능한 산-염기 연쇄 반응 촉매의 합성법에 대하여 연구하였다. 자성을 띄는 다공성 실리카 담체의 합성과 산-염기 촉매의 담지는 모두 하나의 반응기에서 이루어 졌고,

합성된 촉매는 산-염기 연쇄 반응에서 매우 우수한 성능을 보였다. 이 촉매는 자성을 이용하여 손쉽게 분리 될 수 있었고, 연속된 재사용에서도 별도의 재생이나 교체 없이 그 우수한 성능이 유지 되었으며, 또한 촉매 기공의 크기 조절을 통해 반응속도 향상이 가능했다.

다음은 전기화학촉매에 대한 연구로, 질소가 도핑 된 탄소막을 씌운, 금속간 배열이 규칙적인 PtFe 나노입자의 합성에 대하여 연구하였다. 질소가 도핑 된 탄소막은 금속간 배열이 규칙적이지 않은 PtFe 나노입자를 규칙적인 배열을 가진 PtFe 나노입자로 변형시킬 때 필수적인 고온의 열처리 과정에서 나노입자간의 뭉침 현상을 막아주는 것과, 연료전지 운행과정에서 나노입자가 용해되거나 파쇄되는 것을 막아주는 두 가지 목적을 동시에 성공적으로 수행할 수 있음을 보여주었다. 합성된 질소가 도핑 된 탄소막을 씌운, 금속간 배열이 규칙적인 PtFe 나노입자는 연료전지 운행 실험에서 질량 당 활성과 단위면적 당 활성이 모두 상용화 된 백금에 비해 10배 이상 향상된 성능을 보였다. 또한, 100시간의 장기 성능실험에서도 백금 촉매에서는 현저한 성능저하가 나타난 반면, 질소가 도핑 된 탄소막을 씌운, 금속간 배열이 규칙적인

PtFe 나노입자의 경우는 성능의 저하가 매우 적은 것으로 나타났다.

주요어: 나노촉매, 내구성, 협력촉매, 전기촉매, 연쇄반응, 연료전지, 산소환원반응

학 번: 2009-23956